From $NaZn_4Sb_3$ to *HT*-$Na_{1-x}Zn_{4-y}Sb_3$: panoramic hydride synthesis, structural diversity, and thermoelectric properties

Volodymyr Gvozdetskyi,[1] Bryan Owens-Baird,[1,2] Sangki Hong,[1] Tori Cox,[1] Gourab Bhaskar,[1] Colin Harmer,[1,2] Yang Sun,[2] Feng Zhang,[2] Cai-Zhuang Wang,[2,3] Kai-Ming Ho,[2,3] Julia V. Zaikina[1*]

[1] Department of Chemistry, Iowa State University, Ames, Iowa 50011, United States

[2] Ames Laboratory, U.S. Department of Energy, Ames, Iowa 50011, United States

[3] Department of Physics, Iowa State University, Ames, Iowa 50011, United States

Abstract

Two new sodium zinc antimonides $NaZn_4Sb_3$ and *HT*-$Na_{1-x}Zn_{4-y}Sb_3$ were synthesized by using reactive sodium hydride, NaH, as a precursor. The hydride route provides uniform mixing and comprehensive control over the composition, facilitating fast reactions and high-purity samples, whereas traditional synthesis using sodium metal results in inhomogeneous samples with a significant fraction of the more stable NaZnSb compound. $NaZn_4Sb_3$ crystalizes in the hexagonal $P6_3/mmc$ space group (*No*. 194, Z = 2, a = 4.43579(4) Å, c = 23.41553(9) Å), and is stable upon heating in vacuum up to 736 K. The layered crystal structure of $NaZn_4Sb_3$ is related to the structure of the well-studied thermoelectric antimonides $AeZn_2Sb_2$ (*Ae* = Ca, Sr, Eu). Upon heating in vacuum $NaZn_4Sb_3$ transforms to *HT*-$Na_{1-x}Zn_{4-y}Sb_3$ (x = 0.047(3), y = 0.135(1)) due to partial Na/Zn evaporation/elimination, as was determined from high-temperature *in-situ* synchrotron powder X-ray diffraction. *HT*-$Na_{1-x}Zn_{4-y}Sb_3$ has a complex monoclinic structure with considerable degrees of structural disorder ($P2_1/c$ (No. 14, Z = 32), a = 19.5366(7) Å, b = 14.7410(5) Å, c = 20.7808(7) Å, β = 90.317(2)°) and is stable exclusively in a narrow temperature range of 736 – 885 K. Further heating of *HT*-$Na_{1-x}Zn_{4-y}Sb_3$ leads to a reversible transformation to NaZnSb above 883 K. Both compounds exhibit similarly low thermal conductivity at room temperature (0.9 $W \cdot m^{-1} K^{-1}$) and positive Seebeck coefficients (38–52 μV/K) indicative of holes as the main charge carriers. However, resistivities of the two phases differ by two orders of magnitude.

Introduction

Preparation of the compounds, especially new phases, is oftentimes a bottleneck in the material discovery process. Computational predictions regarding stability, structures and properties of novel compounds are proposed to guide experimentalists, but in order to accelerate materials discovery they should be verified by the targeted synthesis of new compounds [1-7]. The vast number of synthesis parameters (*e.g.* temperature, pressure, composition, annealing time, cooling/heating rates), as well as kinetic limitations make unguided solid-state synthesis serendipitous. In addition to the compositional space, the synthesis temperature is a decisive factor in the stabilization of a particular compound. In recent years, the advances in *in-situ* X-ray and neutron diffraction and *in-situ* TEM methods for reaction monitoring, allow a better understanding of the mechanisms in solid-state reactions [3, 8-17]. For instance, high-temperature X-ray diffraction data of the Cs/Sn/P/Se systems gave a "panoramic" view of the compositional phase space and allowed for the discovery of multiple new phases [3]. Unprecedented photon density and high resolution of synchrotron experiments have yielded high-quality data in a short timeframe, which allows for precise study of relationships among phases upon heating or cooling within a very narrow temperature gradient. Using such methods, "blind" synthetic pathway become clear and high-temperature intermediates detected from high-temperature X-ray diffraction can be further prepared *ex-situ*.

Hydride synthetic route, which uses mixable salt-like hydride precursors (*e.g.* alkali metal hydrides AH, A = Li, Na, K), instead of ductile alkali metals was successfully utilized for the synthesis of binary and ternary borides [7, 18-19], antimonides [20-21], arsenides [22-23], silicides [24-27], and germanides [24, 28]. This method is particularly applicable for the compositional screening in the discovery of new ternary alkali zinc antimonides, providing composition control and high purity samples [20]. Traditional solid state synthesis using alkali metal precursors is hampered by their ductility, high reactivity and vapor pressure at elevated temperatures, as well as side reactions with crucible materials. Ductility of alkali metals prevents the intimate mixing of precursors, which oftentimes results in the inhomogeneous samples and impedes compositional control.

Interest in ternary Zintl phase antimonides [29-33] stems primarily from the promising thermoelectric properties of some of the members of this vast family of the compounds, such as $AeZn_2Sb_2$ (*Ae* = Ca, Sr, Ba, Eu, or Yb) [34-35] and $Yb_{14}MnSb_{11}$ [35-37]. Structural and compositional diversity of ternary antimonides containing transition or post-transition metals together with electropositive cations suggests that there are a number of undiscovered related phases with potentially enhanced properties. The hydride synthesis route allows for fast screening of compositional space for different systems at a chosen synthetic temperature. On the other hand, metastable intermediates or phases, which are stable only in narrow temperature range, could be hidden.

Here, we have explored the ternary Na–Zn–Sb system and discovered two new compositionally similar, but structurally different ternary antimonides, both are featuring new structure types. Using the fast hydride route coupled with *in-situ* high-temperature powder X-ray diffraction experiments, compositional and temperature screening allowed for synthesis of two new ternary phases: $NaZn_4Sb_3$ phase and what at first appeared to be its polymorph, but in fact it is a different compound with slightly Na/Zn depleted composition *HT*-$Na_{1-x}Zn_{4-y}Sb_3$, stable in narrow temperature range. The hydride route yields single phase samples of both antimonides, allowing for the experimental access to their transport properties. The crystal structures, synthesis, structural transformations, and transport properties of the $NaZn_4Sb_3$ and *HT*-$Na_{1-x}Zn_{4-y}Sb_3$ are discussed herein.

Experimental

Synthesis. Starting materials for synthesis were used as received: sodium hydride (Sigma-Aldrich, 95%), sodium metal (Alfa Aesar, 99.95%), zinc powder (Alfa Aesar, 99.996%), and antimony lump (Alfa Aesar, 99.9999%). All manipulations of reagents and samples were carried out under an inert argon atmosphere ($p(O_2) < 1$ ppm, $p(H_2O) < 1$ ppm) in a glove box (LC-Technology).

Hydride route. Fine antimony powders were prepared beforehand by ball-milling antimony lumps for 12 min in ambient atmosphere using a standard grinding set with tungsten carbide inserts and high-energy ball-mill SPEX 8000M MIXER/MILL. Afterwards, powders of the sodium hydride, zinc, and antimony were weighted in a 1.03:4:3 molar ratio (m = 0.7 g) and loaded into a polycarbonate grinding set with a methacrylate grinding ball. The vial was further sealed into two plastic bags under argon atmosphere, and removed from the glovebox for ball-milling. Samples were ball-milled for 12 min to achieve sufficient mixing, while longer ball-milling caused partial decomposition of NaH. Inside the glovebox, freshly prepared fine powders were loaded into tantalum containers, which were sealed shut by arc-welding. The sealed tantalum ampoules were removed from the glove box and placed into silica reactors equipped with Swagelok safety check valves to prevent over-pressurizing of the reactors due to hydrogen gas release during the heat treatment. The silica reactors were evacuated to 4×10^{-5} Bar and placed into a resistance furnace (Thermo Scientific Thermolyne Type FD1500M) equipped with a temperature controller (Eurotherm 3216). Samples were slowly (1.4 K/min) heated from room temperature to 723 K, held at that temperature for 8 h, and cooled to room temperature naturally by switching off the furnace. Phase-pure $NaZn_4Sb_3$ compound can be prepared ~~with high purity~~ by following the synthetic method described above. Quenching samples with a Na:Zn:Sb molar ratio of 1.03:4:3 in tantalum containers from higher temperatures (800 K) did not allow the stabilization of *HT*-$Na_{1-x}Zn_{4-y}Sb_3$. For synthesis of *HT*-$Na_{1-x}Zn_{4-y}Sb_3$ phase, powders of $NaZn_4Sb_3$ phase were loaded into graphitized silica tubes (5 mm diameter, 7 cm length), evacuated to 4×10^{-5} bar, flame-sealed, and rapidly heated from room temperature to 800 K (8.4 K/min), held there for 30 min (allowing for partial Na/Zn elimination), and quenched into cold water. Alternatively, *HT*-$Na_{1-x}Zn_{4-y}Sb_3$ phase can be prepared using the hydride route in tantalum containers, with a Na and Zn depleted (~10%) composition, *i.e.* a NaH:Zn:Sb molar ratio of 0.93:3.61:3. Samples were slowly (1.7 K/min) heated from room temperature to 800 K, held at that temperature for 8 h, and quenched into cold water. Both compounds are air- and moisture-stable but were stored in glovebox for further manipulations.

Synthesis from elements: single crystals growth. To obtain crystals suitable for single crystal X-ray diffraction, ~~direct~~ synthesis from elements and heating profile with a slow cooling step was employed. A molar ratio of Na:Zn:Sb = 1.7:4.7:3 with a considerable excess of both Na and Zn was utilized, since samples

with compositions closer to stoichiometric 1:4:3 molar ratio always contained considerable amount of NaZnSb and binary zinc antimonides as impurities. For single crystal growth of the $NaZn_4Sb_3$ compound, elemental Na, Zn, and Sb were loaded into a graphitized silica tube, flame-sealed under vacuum, and heated from room temperature to 923 K (2.1 K/min), held at that temperature for 24 h, cooled to 473 K at a rate of 0.04 K/min, and cooled to room temperature by switching the furnace off. The same molar ratio 1.7:4.7:3 was utilized for single crystal growth of the *HT* phase. The mixture was heated from room temperature to 873 K (2.4 K/min), held at that temperature for 12 h, cooled to 800 K at a rate of 0.015 K/min, and rapidly quenched in cold water. Single crystals of the $NaZn_4Sb_3$ or *HT*-$Na_{1-x}Zn_{4-y}Sb_3$ compounds were mechanically separated from the powders of NaZnSb, additionally traces of binary zinc antimonides were present as impurities within the samples.

Characterization.

Laboratory Powder X-ray Diffraction (PXRD). The purity of polycrystalline samples was checked by means of Rigaku MiniFlex600 powder diffractometer with Cu $K\alpha$ radiation (λ = 1.540593 Å) and Ni-K_β filter. Data were collected on a zero-background plate holder in air at room temperature. Phase analysis was performed using the PDF-2 database incorporated into PDXL program software [38].

Single-Crystal X-ray Diffraction (SC-XRD). Single crystal data were collected by means of Bruker D8 VENTURE diffractometer (Photon CMOS detector, Mo-IμS microsource and Oxford Cryosystem 800 low temperature device) at 100 K for crystals of $NaZn_4Sb_3$ and *HT*-$Na_{1-x}Zn_{4-y}Sb_3$. Data integration, absorption correction, and unit cell determination was performed by APEX 3 software [39]. The starting atomic parameters were obtained by direct methods with the SHELXS-2017 [38]. Subsequently, the structures were refined using SHELXL-2017 [39] (full-matrix least-squares on F_o^2).

$NaZn_4Sb_3$. Crystals of $NaZn_4Sb_3$ phase were found to be extensively twinned and/or weakly diffracting, hardly suitable for SC-XRD. Only basic crystallographic parameters, *i.e.* syngony, cell dimensions, and tentative structural model, though with reasonable interatomic distances, were extracted from experimental single crystal X-ray diffraction data. Due to weak intensity of reflections and insufficient crystal quality, the tentative structure solution was obtained first in triclinic syngony (space group $P\bar{1}$). The further symmetry analysis of atomic coordinates model using Platon software package (command ADDSYM) [41] indicates that the actual symmetry of the structure is hexagonal, space group $P6_3/mmc$ (*No*. 194, Z = 2), a = 4.43579(4) Å, c = 23.41553(9) Å, V = 399.003(5) Å^3. This structural model was further used for Rietveld refinement from high-resolution synchrotron powder X-ray diffraction data (Table S1, Figure S1, Table 2).

HT-$Na_{1-x}Zn_{4-y}Sb_3$. Crystals of *HT*-$Na_{1-x}Zn_{4-y}Sb_3$ phase were considerably larger and stronger diffracting then those of $NaZn_4Sb_3$. Analysis of the diffraction data revealed pseudo-orthorhombic symmetry, *e.g.* monoclinic Laue symmetry with the β angle close to 90°, space group $P2_1/c$ (No. 14, Z = 32). The positions of antimony and zinc atoms were obtained from direct methods (SHELXS) [40]. Positions of sodium atoms were located from a combination of least-squares refinement and difference Fourier maps (SHELXL) [40]. While in the determined model the interatomic distances were found to be within the reasonable range, the refinement has R_1 ~6.5%, large inexplicable electron density peaks at the difference Fourier map, and deviation of the *E*-value statistics from 0.97 and 0.74 for ideal centric and acentric distributions (indicative of possible twinning). The data set was analyzed by COSET [42] to determine the twin law, corresponding to the 2-fold rotation around *a*-axis. Further refinement using commands TWIN (1 0 0 0 −1 0 0 0 −1) and BASF in SHELXL allowed to further reduce R_1 values down to ~4%, while twin fraction was refined to ~7%. Further refinement revealed electron density peaks at the difference Fourier map located in a close proximity to the selected Zn or Sb atomic sites, thus the split site model was considered. In this model the sum of site occupancy factors (s.o.f.) for an atomic site and its split counterparts was constrained to 100%, while the atomic displacement parameters (APDs) were constrained to be the same: Sb(17)–Sb(25), Sb(21)–Sb(26), Sb(24)–Sb(27), Zn(16)–Zn(32), Zn(20)–Zn(33), Zn(27)–Zn(34), Zn(29)–Zn(35), Zn(30)–Zn(36), Zn(31)–Zn(37) (Table 3). The refined s.o.f. for split Sb and Zn sites did not exceed 13% and 19%, respectively. Further refinement indicated that atomic displacement parameters (ADPs) for Na(5) and Na(8) sites were unambiguously larger comparing to the six other Na sites, thus, s.o.f. for Na(5) and Na(8) sites was refined and found to have partial occupancy of 84% and 75% respectively. Additionally, Zn(17) and Zn(23) atoms were found to be partially occupied (96.6% and 93.5%). More detailed analysis indicates complex crystallographic disorder that was modeled with series of constrains. For instance, independently refined occupancies of Sb(17), Zn(20) and Zn(17) were found to be same within 3 e.s.d. (estimated standard deviation). Therefore, the final refinement of the occupancies was done with the following constrains: either Sb(17), Zn(20) and Zn(17) atoms (refined s.o.f. 95.5%.) or Sb(25) and Zn(33) atoms (refined s.o.f. of 4.5%) are present. Similar constrains were used for occupancies of Sb(21) and Zn(23), and Sb(24) and Zn(30). In the same manner, occupancies of Na(5) and Zn(31), Na(8), Zn(16) and Zn(27) were constrained to be the same. Details of the data collection and refinement are summarized in Table 1, atomic coordinates, s.o.f. and ADPs are given in Table S2, interatomic distances are listed in Table S3.

Further refinement indicates that atomic displacement parameters (ADPs) for Na(5) and Na(8) sites were unambiguously larger comparing to the six other Na sites, thus, s.o.f. for Na(5) and Na(8) sites was

refined and found to have partial occupancy of 81% in both cases. Details of the data collection and refinement are summarized in Table 1, atomic coordinates, s.o.f. and ADPs are given in Table S2, interatomic distances are listed in Table S3.

Table 1. Experimental details and crystallographic data for the *HT*-$Na_{1-x}Zn_{4-y}Sb_3$ (single crystal X-ray diffraction data, 100 K).

refined composition	$Na_{0.953(3)}Zn_{3.865(1)}Sb_3$
space group, Z	$P2_1/c$, 24
cell parameters: a, Å	19.508(3)
b, Å	14.708(3)
c, Å	20.736(4)
β, °	90.402(5)
V, Å^3	5950(1)
temperature, K	100(2)
density g/cm^3	5.71
wavelength, Å	0.71073 (Mo-K_α)
absorption coeff., mm^{-1}	22.92
min/max transmission	0.039/0.091
θ_{max}, °	28.75
scan mode	continuous
crystal size, mm	0.4×0.3×0.2
measured reflections	104502
independent reflections	15401 (R_{int} = 0.025)
reflections with $F > 2\sigma(F)$	13212 (R_σ = 0.038)
parameters	602
GOF for F^2	1.13
Final R-indices [$F > 2\sigma(F)$]	R_1 = 0.039, wR_2 = 0.086
R-indices (all data)	R_1 = 0.050, wR_2 = 0.091
larg. diff. peak and hole, e/Å^3	2.99 / -1.75
structure solution	direct methods, SHELXS
structure refinement	least-squares, SHELXL

Further details of the crystal structure refinement can be obtained from the Fachinformationszentrum Karlsruhe, 76344 Eggenstein-Leopoldshafen, Germany (fax: (+49)7247-808-666; e-mail: crysdata@fiz-karlsruhe.de) on quoting the depository number CSD 1919785.

Synchrotron Powder X-ray Diffraction. High-resolution synchrotron powder diffraction data were collected at beamline 11-BM Advanced Photon Source (APS), Argonne National Laboratory (ANL) with an average wavelength λ = 0.412804 Å. Data were collected at room temperature and ambient pressure in a Kapton capillary.

High-temperature synchrotron powder X-ray diffraction data (HT-PXRD) was collected at beamline 17-BM (APS ANL) with an average wavelength λ = 0.24130 Å. Powdered samples of $NaZn_4Sb_3$ and *HT*-$Na_{1-x}Zn_{4-y}Sb_3$ were filled in a 0.7 mm outer diameter thick-wall (0.1 mm) silica capillary and sealed under vacuum. The capillary was mounted into a secondary shield capillary (0.9 mm inner diameter, 1.1. mm outer diameter) located on a sample stage equipped with two resistive micro-heaters and a thermocouple set as close as possible to the measurement area. The further details of experimental setup can be found elsewhere [43]. Data were collected upon heating and cooling in the temperature range 298 K→900 K→298 K with a heating and cooling rate of 10 K·min^{-1} and 15 K·min^{-1} for $NaZn_4Sb_3$ and *HT*-$Na_{1-x}Zn_{4-y}Sb_3$, respectively.

Diffraction patterns were analyzed by the Rietveld refinement method using the GSAS II software package [43]. The profile parameters, background parameters, zero correction, and cell parameters were refined first. The background was fitted using a shifted 14 order Chebyshev polynomial function ($NaZn_4Sb_3$) and 24-point linear interpolation (*HT*-$Na_{1-x}Zn_{4-y}Sb_3$), a pseudo-Voigt function was applied to generate the profile shape, the preferential orientation of crystallites was taken into account. Due to the complexity of the structure of *HT*-$Na_{1-x}Zn_{4-y}Sb_3$ phase and presence of light elements (Na, Zn) together with heavy element (Sb), the refinement of all atomic parameters cannot be reliably performed from powder X-ray diffraction data (data/parameters), but full profile fitting using the model determined from the single crystal X-ray diffraction results in low R_B = 12 %, indicating its validity (Tables S1, Figure S2).

Spark-Plasma Sintering. Samples of $NaZn_4Sb_3$ and *HT*-$Na_{1-x}Zn_{4-y}Sb_3$ prepared via hydride route were further consolidated into dense pellets using Spark Plasma Sintering (SPS). In the argon-filled glovebox, the powdered samples were loaded into a small graphite die (inner diameter 5 mm) between several circles of graphite foil and enclosed with tungsten carbide plungers. The smaller die was assembled, inserted into larger outer graphite die with graphite plungers (inner diameter 20 mm) and further transported to SPS-machine Dr. Sinter Lab Jr. SPS-211Lx (Sumitomo Coal Mining Co., Ltd.) keeping the assembly under inert atmosphere. The samples were sintered by slow heating to 448 K over a period of 10 min under a uniaxial pressure of 90 MPa and dwelling for 5 min. Afterwards, the pressure was released, and sintered pellets were

allowed to cool to room temperature without application of pressure. The pellets were removed from the graphite dies and polished to remove traces of the graphite foil. The geometrical densities of the pellets were ~ 85 % and 81 % for $NaZn_4Sb_3$ and *HT*-$Na_{1-x}Zn_{4-y}Sb_3$ phases, respectively, compared to the theoretical X-ray densities. Binary ZnSb was detected as impurity (7 wt. %) in sintered pellet of $NaZn_4Sb_3$ phase.

Elemental Analysis. Elemental analysis was performed by means of EI Quanta-250 field emission scanning electron microscope (SEM) equipped with an Oxford X-Max 80 detector and an Oxford Aztec energy-dispersive X-ray analysis system. Inside glove box small pieces of the pellets sintered by SPS were mounted onto an aluminum holder designed for air-sensitive samples using double-sided carbon tape, oriented with a flat face perpendicular to the beam and analyzed using a 15 kV accelerating voltage and an accumulation time of 60 s.

Thermoelectric Properties Measurement. Transport properties of pellets prepared by SPS were measured in the temperature range of 10–300 K using the commercial multipurpose Physical Properties Measurement System Evercool II (PPMS, Quantum Design). The Seebeck thermopower and thermal conductivity were measured using the Thermal Transport Option (TTO) in a two-probe configuration. Electrical resistivity was measured using the Alternating Current Transport (ACT) option and a four-probe geometry using 50 μm platinum wires attached with silver paste.

Differential Scanning Calorimetry-Thermal Gravimetry Analysis (DSC-TGA). To evaluate the thermal stability of the phases, a differential scanning calorimetry (DSC) measurement was performed using a Netzsch 404 F3 Pegasus Differential Scanning Calorimeter. Powdered samples of $NaZn_4Sb_3$ and *HT*-$Na_{1-x}Zn_{4-y}Sb_3$ ($m \cong 50$ mg) were sealed inside an evacuated silica ampoule, heated to 873 K, and cooled to room temperature with a rate of 10 K/min rate. In a separate run, the thermal stability of a powdered samples of $NaZn_4Sb_3$ ($m = 12.14$ mg) and *HT*-$Na_{1-x}Zn_{4-y}Sb_3$ ($m = 11.05$ mg) were checked by DSC/TGA measurement in an alumina Al_2O_3 pan-type crucible with a lid using a Netzsch STA449 F1 Jupiter. Samples were heated to 900 K and cooled to room temperature with a 10 K/min rate under a flow of argon.

Computational details. First-principles calculations were carried out based on density functional theory (DFT) using VASP code [44-46]. The projected augmented-wave (PAW) method [47] was used to describe the electron-ion interaction, and the generalized gradient approximation (GGA) in the Predew-Burke-Ernzerhof (PBE) form [48] was employed for the exchange-correlation energy functional. A plane-wave basis with a kinetic energy cutoff of 520 eV was used. Only the Γ-point was used to perform the Brillouin zone integration for the large unit cell with the composition $Na_{32}Zn_{124}Sb_{96}$ containing 252 atoms. All atoms in the calculation cell were allowed to relax until the forces on each atom is smaller than 0.01 eV/Å.

Results and discussion.

In the ternary system Na–Zn–Sb, only NaZnSb (PbClF or Cu_2Sb structure type, *P*4/*nmm*) has been previously reported [49-50]. Recently, we have successfully utilized hydride route for preparation of complex solids, including antimonides [19-20], which are hardly accessible by traditional methods of synthesis. The hydride route utilizes brittle salt-like alkali metal hydride precursors (LiH, NaH, KH) instead of ductile and soft alkali metals. This method facilitates thorough mixing of the reactants, allowing for comprehensive control over the alkali metal concentration, thus providing an exceptional purity of products and fast reaction kinetics. Furthermore, it can be used for fast screening of multicomponent systems allowing identification of new compounds with specific chemical composition. For example, in the K–Zn–Sb system, in which only KZnSb has been previously reported [49-50], we recently obtained new compound $K_{8-x}Zn_{18+3x}Sb_{16}$ with high purity using the hydride method [19], while synthesis from elements resulted in inhomogeneous samples with considerable fraction of thermodynamically stable KZnSb.

When the same hydride synthesis is applied in the Na–Zn–Sb system, we identified $NaZn_4Sb_3$, which subsequently led to the discovery of the *HT*-$Na_{1-x}Zn_{4-y}Sb_3$ phase. The composition $NaZn_4Sb_3$ is located directly on the line connecting Na and binary Zn_4Sb_3 or $Zn_{13-\delta}Sb_{10}$ in the ternary phase diagram. Interestingly, Zn_4Sb_3 or $Zn_{13-\delta}Sb_3$ exhibits complex temperature-driven phase transitions $\alpha' \rightarrow \alpha \rightarrow \beta \rightarrow \gamma$ followed by melting at 841 K [51-55]. From the structural point of view, the phase transitions in Zn_4Sb_3 occur because of the ordering of Zn interstitial atoms and vacancies and is accompanied by the slight variation in Zn composition [51-55]. Structural polymorphism is retained, when Na is introduced to the Zn_4Sb_3 structure, as two polymorphic-like compounds can be stabilized: $NaZn_4Sb_3$ and another phase (referred to as *HT*-$Na_{1-x}Zn_{4-y}Sb_3$). The latter shows a deviation from the 1:4:3 composition and is stable in a narrow temperature range, thus can only be prepared by quenching from high temperatures.

Crystal structure of $NaZn_4Sb_3$. Synthesis from Na, Zn, and Sb elements in a 1.03:4:3 molar ratio resulted in inhomogeneous samples, where NaZnSb was a major product. On the contrary, the single-phase sample of $NaZn_4Sb_3$ can be prepared using NaH, Zn, and Sb mixed in a 1.03:4:3 molar ratio. Synthesis from elements always resulted in inhomogeneous multiphase samples, thus the compositions utilized for single crystal growth deviate from 1:4:3. Single crystals of targeted $NaZn_4Sb_3$ phase were selected from the multiphase sample with nominal molar ratio of Na:Zn:Sb = 1.7:4.7:3; samples with composition closer to stoichiometric 1:4:3 molar ratio (*e.g.* 1.3:4.3:3) contained substantial amounts of NaZnSb and binary zinc antimonides as impurities making harvesting of crystals challenging (Figure S3). The tentative crystal structure model was first obtained from single crystal X-ray diffraction, but the crystals were of poor quality. The obtained model was further refined using synchrotron powder X-ray diffraction data (Table 1 and S1).

$NaZn_4Sb_3$ has a layered crystal structure (*P*6$_3$/*mmc, hP*16, a = 4.43579(4) Å, c = 23.41553(9) Å, Z = 2) (Figure 1). Search by Pearson symbol, unit cell metric, and Wyckoff sequence (f^3da) of the Inorganic Structure database (ICSD) indicates that this is a new structure type, although its crystal structure is closely related to other ternary zinc antimonides [56], as discussed below. In the structure of $NaZn_4Sb_3$, Zn atoms occupy two 4*f* sites, Sb atoms on one 4*f* and one 2*d* sites, while a single Na 2*a* site is present (Table 2). The layered structure of $NaZn_4Sb_3$ can be viewed as anionic $[Zn_4Sb_3]^-$ slabs sandwiched between a single layer of Na^+ cations. Within the anionic $[Zn_4Sb_3]^-$ slab there are two types of Zn atoms: Zn(2) with a distorted tetrahedral coordination by four Sb atoms at a distances of 2.57 Å and 2.86 Å (×3) and Zn(1) with a trigonal pyramidal coordination by three Sb atoms at a distance of 2.65 Å. A fourth Sb atom is present for Zn(1), but is located at a considerably longer distance, ~3.18 Å. The two antimony atoms have considerably different environments as well: Sb(1) (4*f* site) is in an "inverted tetrahedron" or "umbrella-like" coordination capping the surface of the slab by four Zn atoms at a distance of 2.65 Å (×3) and 2.57 Å, and additionally, it has 3 Na atoms at a distance of 3.26 Å. Sb(2) (2*d* site) is in a trigonal prismatic coordination at the center of the slab by six Zn atoms at a distance of 2.86 Å. These distances are within the range for typical Zn–Sb distances in other ternary alkali metal zinc antimonides [52], such as NaZnSb (2.76 Å) [20, 50], KZnSb (2.62 Å) [50], $K_{8-x}Zn_{18+3x}Sb_{16}$ (2.63–2.95 Å) [19], *hex*-LiZnSb (2.67–2.76 Å) [57], $Rb_2Zn_5Sb_4$ (2.64–2.90 Å at 200 K) [58], as well as in binary zinc antimonides, such as ZnSb (2.64–2.90 Å) [59], Zn_4Sb_3 (2.55–2.98 Å) [51], and β-Zn_8Sb_7 (2.63-3.15 Å) [60].

The structure of $NaZn_4Sb_3$ is related to the well-studied *Ae*Zn_2Sb_2 (*Ae* = Ca, Sr, Eu, Yb) family [33-34] with Ce_2SO_2 structure type ($P\bar{3}m$, *hP5,* for *Ae* = Ca a = 4.441 Å; c = 7.464 Å) as well as to the *A*Cd_4Pn_3 and *A*Zn_4Pn_3 phases (*A* = Na, K, Rb, Cs; *Pn* = As, P) with $NaZn_4As_3$ structure type ($R\bar{3}m$; *hR*8, for $NaZn_4As_3$: a = 4.1694 Å; c = 32.86 Å) [61]. Disregarding the trigonal pyramidal coordination of Zn(1) atom, the anionic $[Zn_4Sb_3]^-$ slab in the structure of $NaZn_4Sb_3$ can be viewed as a layer of edge-sharing $ZnSb_4$ tetrahedra in the *ab*-plane, similar to that in *Ae*Zn_2Sb_2. Unlike the *Ae*Zn_2Sb_2 structure, the $[Zn_2Sb_2]$ layers are further linked by sharing common Sb atoms into $[Zn_4Sb_3]$ slabs. In fact, the structure of $NaZn_4Sb_3$ can be derived from the $CaZn_2Sb_2$ structure (Figure 1 and 2a), where every other Ca layer is removed and the adjacent $[Zn_2Sb_2]$ layers are shifted and condensed into a single slab accompanied with removal of one Sb layer (Figure 2a). The resultant $[Zn_4Sb_3]$ slab in $NaZn_4Sb_3$ is comparable to that of $[Zn_4As_3]$ in $NaZn_4As_3$ (Figure 1 left) [61]. Unlike $NaZn_4Sb_3$, the two Zn atoms in adjacent tetrahedral $ZnAs_4$ units are not aligned, leading to different central Sb atom coordination: trigonal prismatic in the case of $NaZn_4Sb_3$ and trigonal antiprismatic in $NaZn_4As_3$ (Figure 2b). Furthermore, the stacking sequence of $[Zn_4(As/Sb)_3]$ slabs is different: in $NaZn_4As_3$ the adjacent $[Zn_4As_3]$ slabs are shifted by 1/3 in the *ab*-plane, to produce a *R*-centered

trigonal unit cell; while in $NaZn_4Sb_3$ two $[Zn_4Sb_3]$ slabs are related by an inversion center with hexagonal layers of Na^+ cations in between. Therefore, the $NaZn_4Sb_3$ is a new representative for the family of Zintl phases which adopts a 1:4:3 stoichiometry but has its own unique layered crystal structure.

Considering Na and Zn as +1 and +2 cations, respectively, and the electronegative Sb having −3 oxidation state, the valence electron count for $NaZn_4Sb_3$ yields electron-balanced composition $Na^+(Zn^{+2})_4(Sb^{-3})_3$.

Table 2. Atomic coordinates and isotropic displacement parameters of $NaZn_4Sb_3$ ($P6_3/mmc$, $hP16$, a = 4.43579(4) Å, c = 23.41553(9) Å) synchrotron data, 298 K.

Site	Wyckoff site	x	y	z	U_{iso}, Å^2
Sb(1)	4*f*	⅓	⅔	0.08580(4)	0.0105(2)
Sb(2)	2*d*	⅓	⅔	¾	0.0220(3)
Zn(1)	4*f*	⅓	⅔	0.61404(5)	0.0350(4)
Zn(2)	4*f*	⅓	⅔	0.19542(5)	0.0361(3)
Na	2*a*	0	0	0	0.112(3)

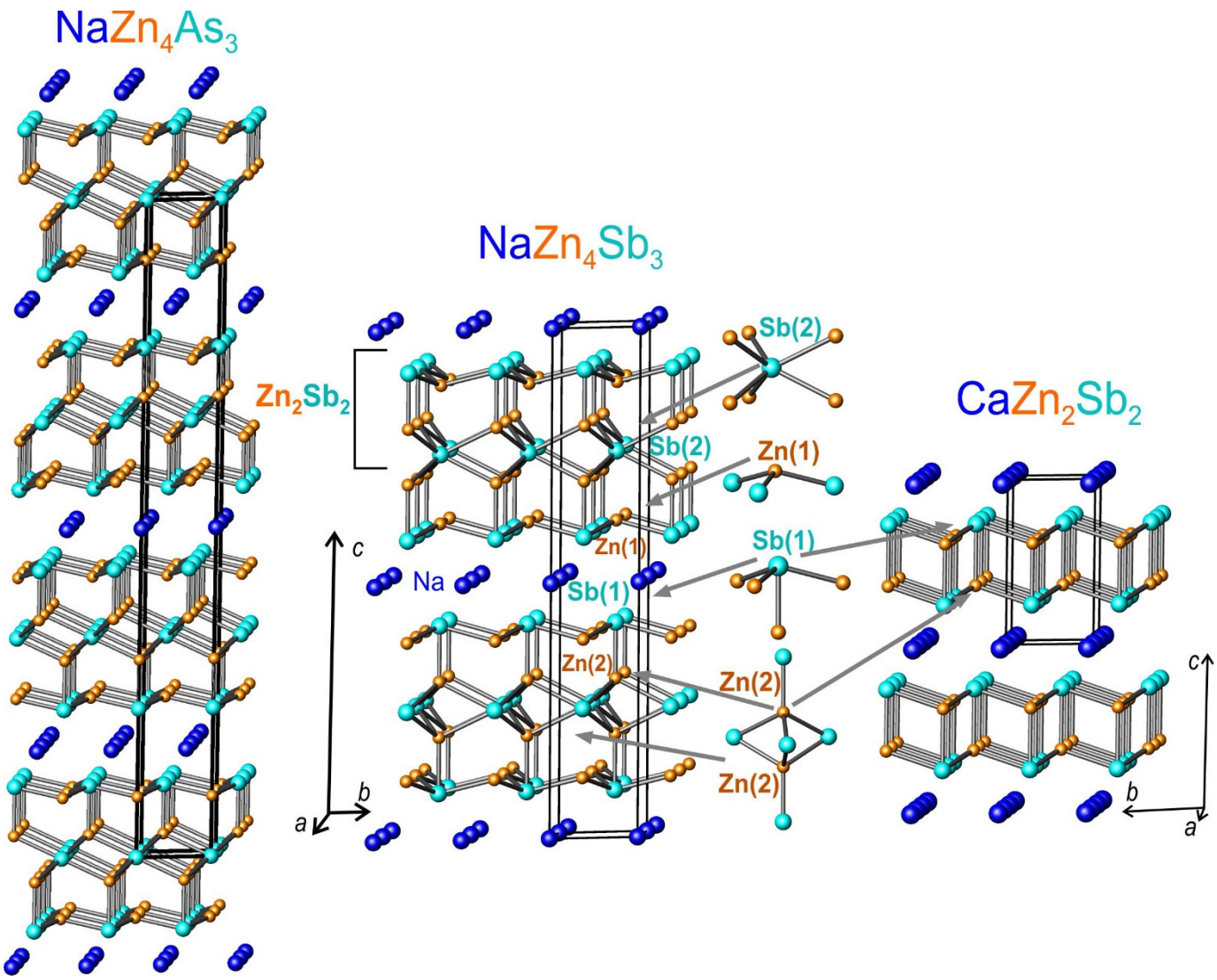

Figure 1. Crystal structure of $NaZn_4Sb_3$ in comparison with structure of $NaZn_4As_3$ (left) and $CaZn_2Sb_2$ (right). The coordination of Zn and Sb atoms is emphasized; Na(Ca) – blue, Zn – orange, Sb(As) – cyan.

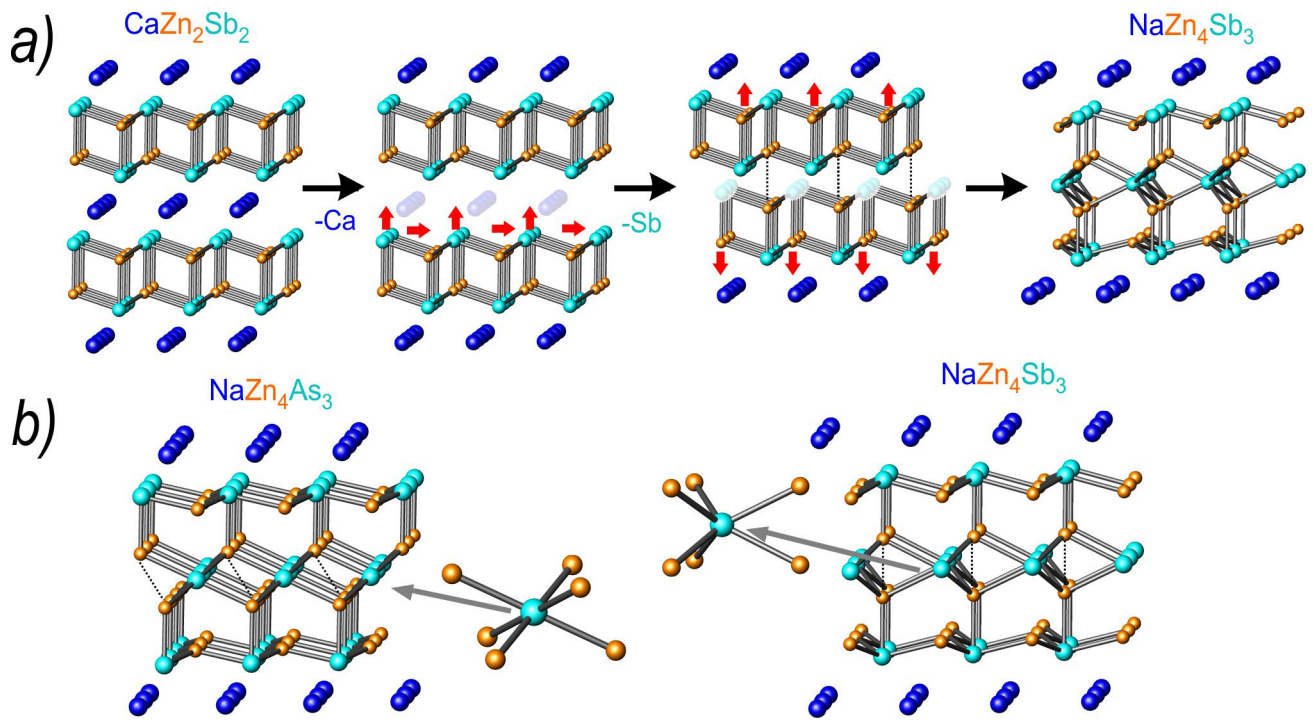

Figure 2. a) Schematic showing transformation of $[Zn_2Sb_2]$ layer found in the $CaZn_2Sb_2$ structure into $[Zn_4Sb_3]$ layer in structure of $NaZn_4Sb_3$; b) Structural comparison of anionic slabs $[Zn_4As_3]$ and $[Zn_4Sb_3]$; dashed line emphasizes the alignment of Zn atoms within two stacked $Zn(As/Sb)_4$ tetrahedral units. The difference in coordination polyhedral for Sb(As) is shown. Na(Ca) – blue, Zn – orange, Sb(As) – cyan.

Reversible $NaZn_4Sb_3$ to HT-$Na_{1-x}Zn_{4-y}Sb_3$ transformation by in-situ HT-PXRD. High-temperature synchrotron powder X-ray diffraction (HT-PXRD) of the $NaZn_4Sb_3$ sample sealed under vacuum in a silica capillary indicates its structural transformation into the *HT*-$Na_{1-x}Zn_{4-y}Sb_3$ phase at ~736 K (Figure 3). Binary ZnSb begins to emerge at ~500 K upon heating, indicating partial Na elimination as a result of side reaction with the silica, but disappears (melts) above 736 K. With further heating of *HT*-$Na_{1-x}Zn_{4-y}Sb_3$ above 885 K, the sample converts to NaZnSb and melt. Upon cooling from 900 K, the reversible transformation takes place: NaZnSb + melt → *HT*-$Na_{1-x}Zn_{4-y}Sb_3$ at 885 K → $NaZn_4Sb_3$ at 720 K. It should be noted that according to the HT-PXRD data, the *HT*-phase exists exclusively in the narrow temperature range 736-885 K. With the increasing of temperature above ~736 K formation of the *HT*-phase is driven by Na/Zn elimination, and as a result its content is increasing, while fraction of $NaZn_4Sb_3$-phase is decreasing. Above 810 K, traces of NaZnSb appear, which becomes more pronounced above 885 K when the *HT*-phase completely decomposes. By comparing two PXRD patterns collected at 373 K on heating and cooling steps, the cooling step contains $NaZn_4Sb_3$ (~86%) with more impurities, such as NaZnSb, ZnSb, and unassigned peaks,

compared to heating data (*i.e.* initial sample). This suggests a shift in composition from the initial Na:Zn:Sb 1:4:3 ratio and partial decomposition of $NaZn_4Sb_3$ phase upon heating (Figure 3, 6).

In-situ high-temperature synchrotron powder X-ray diffraction is very sensitive to phase transitions, as it provides high resolution data, facilitating detection of even small amounts of crystalline phase(s) at different temperatures. Differential scanning calorimetry (DSC) on the other hand is not suitable for systems where many exo- and endothermic reactions take place simultaneously. The Na–Zn–Sb system is an example of such a case, in which samples that are heat treated under vacuum can lead to partial Na/Zn evaporation and possibly side reactions with the containment vessel (silica). DSC data of $NaZn_4Sb_3$ sample in an alumina crucible (Figure S4) indicates an endothermic process, possibly due to its melting or decomposition at ~750 K, followed by a smaller endothermic event at ~800 K, possibly because of NaZnSb formation. Upon heating of the sample in an alumina crucible, a 1% mass loss is observed, which may be due to a slight Na/Zn evaporation. On cooling, two exothermic peaks are observed: less intensive at ~765 K, possibly due the traces of *HT*-$Na_{1-x}Zn_{4-y}Sb_3$ present, as a result in the composition shift, and a more intense peak at ~735 K, when $NaZn_4Sb_3$ is recovered. In turn, DSC data of samples run in silica is in accordance with *in-situ* high-temperature synchrotron powder X-ray diffraction data. However due to side/competing reactions at elevated temperatures, analysis is less sensitive. The PXRD data of the sample after DSC (in sillica) indicates that $NaZn_4Sb_3$ is partially decomposed during the measurement, as peaks of Zn_4Sb_3 and ZnO are evident (Figure S5). This is further evidence that Na elimination processes may be due to a side reaction with the silica vessel.

Synthesis of HT-$Na_{1-x}Zn_{4-y}Sb_3$. Equipped with the knowledge regarding the temperature range, where *HT*-$Na_{1-x}Zn_{4-y}Sb_3$ is stable, its synthesis was performed by quenching of the $NaZn_4Sb_3$ sample in evacuated and sealed silica ampoule from 800 K. Furthermore, *HT*-$Na_{1-x}Zn_{4-y}Sb_3$ compound can be prepared by annealing of NaH, Zn and Sb in the Ta ampoule, but only when Na- and Zn-depleted composition NaH:Zn:Sb = 0.93:3.61:3 (molar ratio) is used, whereas 1.03:4:3 molar ratio always gives $NaZn_4Sb_3$ phase even after quenching from 800 K. This again indicates that during heating of $NaZn_4Sb_3$ in silica tube partial elimination of Na and Zn takes place, probably due to the side reaction of Na with SiO_2, thus shifting the composition toward the Na/Zn depleted facilitates formation of *HT*-$Na_{1-x}Zn_{4-y}Sb_3$. The Na/Zn deficiency in *HT*-$Na_{1-x}Zn_{4-y}Sb_3$ phase was further confirmed by refinement of the crystal structure from single crystal diffraction data and EDX analysis (*vide infra*).

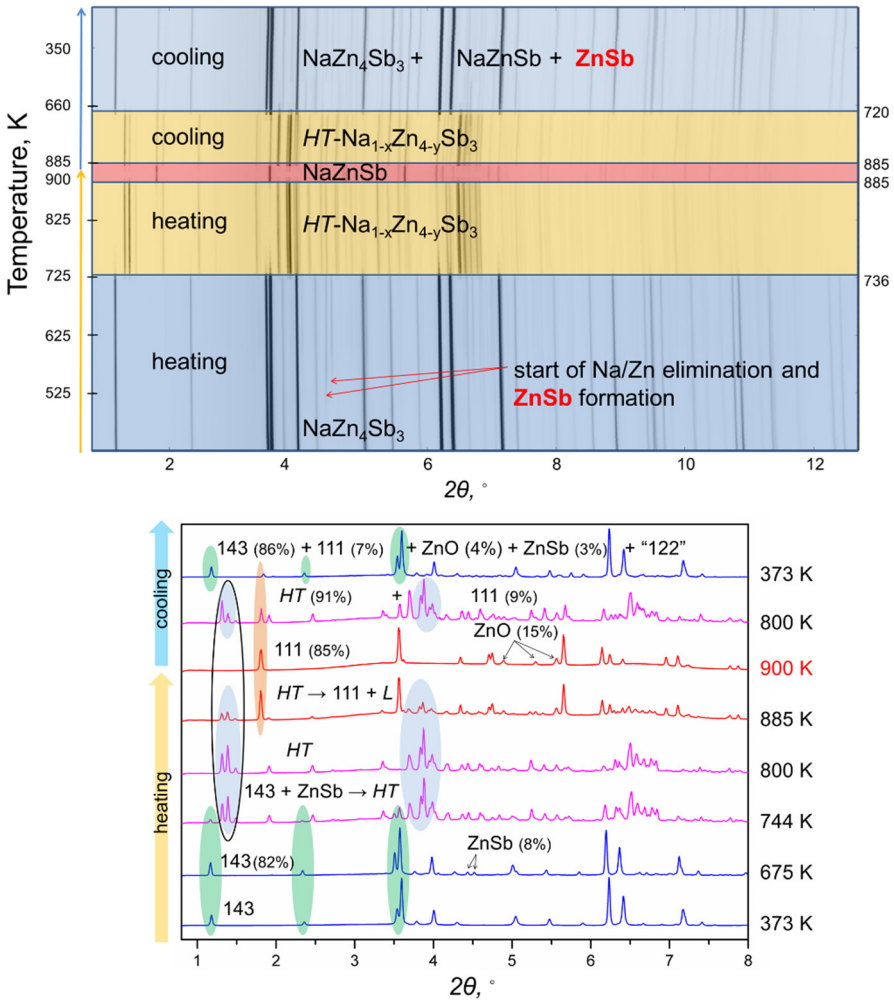

Figure 3. (top) High-temperature *in-situ* powder X-ray diffraction patterns, showing the transformation of powdered sample $NaZn_4Sb_3$ sealed in an evacuated silica capillary. The "waterfall" plot shows the evolution of PXRD patterns with the concomitant change in temperature from room temperature to 900 K followed by subsequent cooling to room temperature. The temperature regions with distinct phase contributions are highlighted in blue/yellow/red; (bottom) Selected high-temperature powder X-ray diffraction patterns showing the products of decomposition/transformation of the $NaZn_4Sb_3$ at different temperatures. Selected groups of peaks as "fingerprints" of the ternary and binary phases are highlighted: green (143) – $NaZn_4Sb_3$; blue (*HT*) – *HT*-$Na_{1-x}Zn_{4-y}Sb_3$; orange (111) – NaZnSb; *L* = liquid; 122 – "$NaZn_2Sb_2$".

Crystal structure of HT-$Na_{1-x}Zn_{4-y}Sb_3$: structural complexity and disorder.

Single crystals were selected from an inhomogeneous sample prepared from the elements in the same nominal composition (Na:Zn:Sb = 1.7:4.7:3) as one used for crystal growth of $NaZn_4Sb_3$ compound; sample

was quenched to stabilize *HT*-$Na_{1-x}Zn_{4-y}Sb_3$. Sample contained considerable fraction of NaZnSb impurity (in a powdery form), while chunks mechanically separated from powders comprise mainly *HT*-$Na_{1-x}Zn_{4-y}Sb_3$ phase (Figure S6). The complex crystal structure (Figure 5) of *HT*-$Na_{1-x}Zn_{4-y}Sb_3$ was determined from single crystal X-ray diffraction data. *HT*-$Na_{1-x}Zn_{4-y}Sb_3$ crystallizes in the monoclinic space group $P2_1/c$ (No. 14, $Z = 32$) and unit cell with monoclinic, pseudo-orthorhombic symmetry (a = 19.508(3) Å, b = 14.708(3) Å, c = 20.736(4) Å, β = 90.402(5)°) (Table 1). The unit cell of the ideal structure contains 96 Sb atoms distributed over 24 4*e*-sites, 124 Zn atoms distributed over 31 4*e*-sites, and 32 Na atoms occupying 8 4*e*-sites (Table 3). Searching of the Inorganic Crystal Structure Database (ICSD) using Pearson symbol (*mP*252), unit cell metrics, and Wyckoff sequence (e^{63}) indicate that this is a new structure type [50].

The structure is organized around Sb chains running along the *b*-axis (Figure 5*a*-*b*). These chains are surrounded by Zn atoms, which are further connected to a second shell of Sb atoms, forming tubular columns along *b*-axis (Figure 5*a* and *c*). Those columns are then linked in the *ac*-plane either via Zn–Sb intercolumnar bonds or via bridging Zn atoms to form a three-dimensional framework with large channels, hosting two columns of Na^+ cations (Figure 5*d*). The Zn–Sb distances range between 2.57 Å–2.94 Å, and are similar to the Zn–Sb distances in other ternary alkali metal zinc antimonides (*vide supra*). The Sb atoms are either 5- or 6-coordinated by Zn atoms, except Sb(8), Sb(14), Sb(16), Sb(18), and Sb(22), which are 3-coordinated (Table S3). Sb atoms surround Na within the channels, and thus are coordinated by 2-4 Na^+ at distances ranging from 3.13 Å to 3.67 Å. The relatively short Na–Sb distances of ~3.13 Å are not typical, but have been reported in other ternary and quaternary sodium antimonides, such as Na_3InSb_2 [62], $Na_2Al_2Sb_3$ [63], Na_5SnSb_3 [64], $K_2NaInSb_2$ [65], $Na_2YbCdSb_2$ [66]. Most of the Zn atoms are in a distorted tetrahedral coordination by four Sb sites, except for zinc atoms residing in split positions.

A considerable degree of disorder occurs within the structure of *HT*-$Na_{1-x}Zn_{4-y}Sb_3$, mainly associated with the Na(5) and Na(8) sites being ~81% occupied, as well as Sb and Zn split sites and two partially occupied zinc sites, Zn(23) and Zn(17) (Figure 5b-d). Split sites within the Sb chain (Figure 5 b-c) evokes additional splitting in adjacent Zn sites. For instance, when Sb(24) is present, it is coordinated by Zn(30), while Sb(27) is coordinated by Zn(36). Likewise Sb(17), Zn(20) and Zn(17) atoms are present (s.o.f. of 95.5%) or Sb(25) and Zn(33) atoms (s.o.f. of 4.5%). The partial occupancy of Na(5) and Na(8) within the channels also leads to the splitting of the adjacent Zn positions, e.g. when Na is absent, Zn atoms slightly move toward the "hole" in the channel: either Na(5) and Zn(31) are present (s.o.f. 81.4%) or Zn(37) (s.o.f. 18.7(9)%). Similarly, when Na(8), Zn(16) and Zn(27) are occupied (s.o.f. 81.2%), then Zn(32) and Zn(34) are absent (s.o.f. 18.8%). Considering structural disorder, the refined composition from single crystal XRD for *HT*-$Na_{1-x}Zn_{4-y}Sb_3$ is $Na_{0.953(3)}Zn_{3.865(1)}Sb_3$, which is consistent with the Na- and Zn-depleted composition needed for synthesis. This refined composition *HT*-$Na_{1-x}Zn_{4-y}Sb_3$ suggests an electron imbalance, when +1

and +2 charges are assigned for Na and Zn, respectively, and the electronegative Sb has a –3 charge: $(Na^{+})_{0.953}(Zn^{+2})_{3.865}(Sb^{-3})_3$ with 0.36 extra electrons per formula unit.

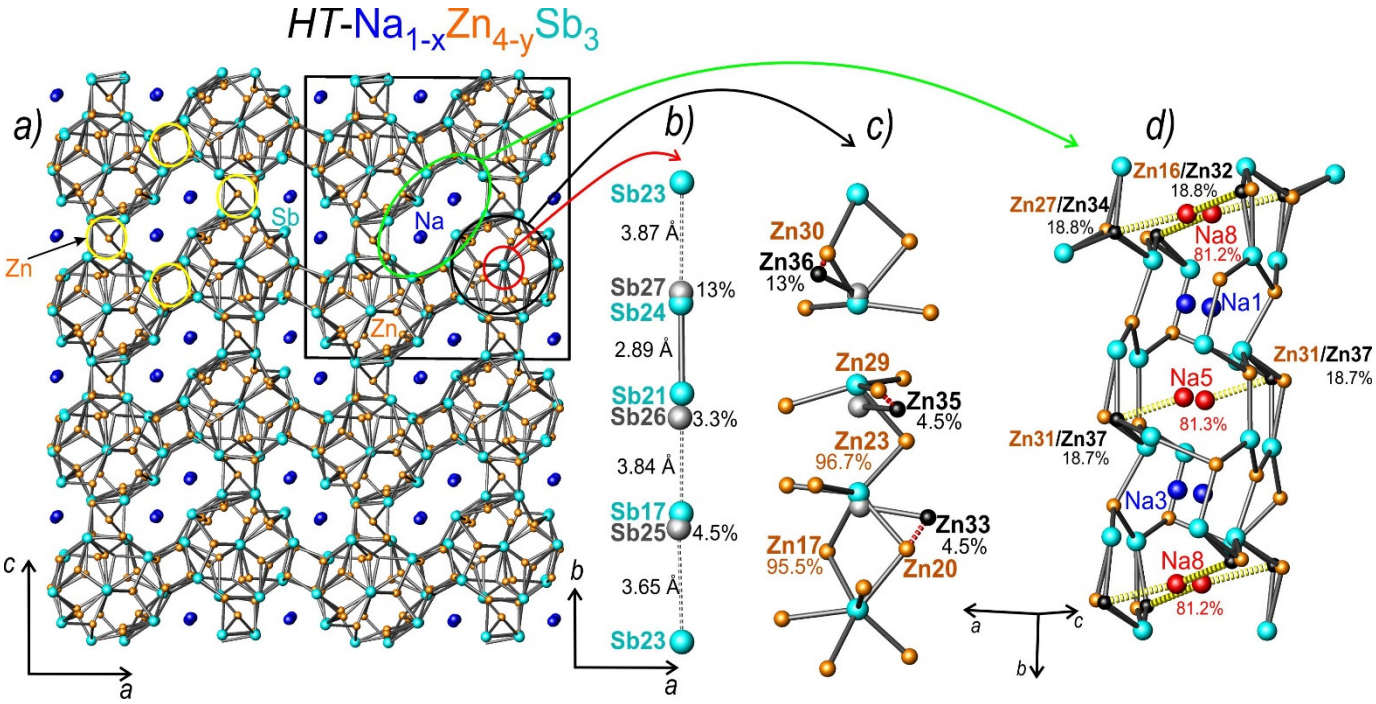

Figure 4. a) Crystal structure of *HT*-$Na_{1-x}Zn_{4-y}Sb_3$ in *ac*-plane: Na – blue, Zn – orange, Sb – cyan. Split sites are not shown, various fragments are highlighted with red (Sb chains), green (Na channels), yellow and black circles; b) Sb chain running along *b*-axis; split Sb sites are show in grey and their s.o.f. is given in %; the bond distances and longer interatomic distances are drawn with solid and dashed lines, respectively; c) Coordination of Sb atoms from the chain by Zn atoms; the split Zn sites are shown in black and their s.o.f. is given in %; the unrealistic Zn–Zn distances due to the split sites are shown with red dashed lines; d) Coordination of Na atoms within the channel; Na with partial occupancy is shown in red together with its s.o.f. (%); the split Zn sites are shown in black and their s.o.f. is given in %; the unrealistic Na–Zn distances due to the split sites are shown with yellow dashed lines; Na–Na distances exceed 3.59 Å.

Vacancy formation in HT-$Na_{1-x}Zn_{4-y}Sb_3$*: computational input.* In order to evaluate the preference for the vacancy formation in the specific Na sites in the structure of *HT*-$Na_{1-x}Zn_{4-y}Sb_3$, the vacancy formation energies (E_{vac}) for various Na sites were calculated by

$$E_{vac} = E(cell_{vac}) + E(Na) - E(cell),$$

where $E(cell)$ and $E(cell_{vac})$ are the total energies of the optimized structures with and without a Na vacancy, respectively. $E(Na)$ is the energy of a Na atom in the bulk phase. The idealized structure model (without

split sites for Sb/Zn) considered for calculations has the composition $Na_{32}Zn_{124}Sb_{96}$ ($\equiv NaZn_{3.875}Sb_3$, *cell*) and was further optimized to yield *E*(*cell*). One Na atom was removed from each of the eight Na sites in succession (Table 3), and the structure with the composition $Na_{31}Zn_{124}Sb_{96}$ ($\equiv Na_{0.96875}Zn_{3.875}Sb_3$, $cell_{vac}$) was optimized to yield $E(cell_{vac})$. A positive value of E_{vac} indicates an energy cost to create the vacancy. As it can be seen from Table 4, vacancies at Na(5) and Na(8) sites have the lowest formation energy compared to other Na sites, which is consistent with the experimentally determined structure from SC XRD with only Na(5) and Na(8) sites exhibiting partial occupancies (Table S2). Furthermore, based on the first-principle calculations, the formation of vacancies at Na(5) and Na(8) sites only causes slight local structural relaxations. The relaxation patterns around vacant Na(5) or Na(8) are rather similar: vacancy formation causes two adjacent Zn atoms and adjacent Na atoms to shift toward the vacancy, while overall structural motif remains unchanged. That is again consistent with the structure solved from SC XRD data (Figure 5 *d*), where vacancies in Na(5) and Na(8) sites cause the splitting of the adjacent Zn sites.

Table 3. Vacancy formation energy at each Na site in the structure of *HT*-$Na_{1-x}Zn_{4-y}Sb_3$. Two sites with the lowest vacancy formation energies are *italicized*.

Site	E_{vac} (eV)
Na(1)	0.788
Na(2)	0.805
Na(3)	0.902
Na(4)	0.913
Na(5)	*0.706*
Na(6)	0.917
Na(7)	0.881
Na(8)	*0.763*

Thermal stability of HT-$Na_{1-x}Zn_{4-y}Sb_3$. High-temperature powder XRD data for the *HT*-$Na_{1-x}Zn_{4-y}Sb_3$ phase indicates multiple transitions upon heating (Figures 6 and 7). A cascade of exothermic peaks is present on the DSC heating curve in alumina crucible at 470–575 K, indicating that *HT*-phase is indeed metastable at room temperature and its early transformation to $NaZn_4Sb_3$ was observed already at 520 K. The metastable nature of *HT*-$Na_{1-x}Zn_{4-y}Sb_3$ was also evident from its decomposition during spark plasma sintering already at 473 K, while sintering at a slightly lower temperature (453 K) resulted in 81% pellet compactness without any discernable changes based on PXRD.

From the *in-situ* high-temperature synchrotron powder XRD data (Figures 5) the *HT*-phase was found to decompose according to the following equation:

HT-$Na_{1-x}Zn_{4-y}Sb_3$ → $NaZn_4Sb_3$ + ZnSb + "$NaZn_2Sb_2$" in the temperature range 470 K–765 K. A new phase detected from synchrotron PXRD data, has composition richer in Na and Sb than 1:4:3; this phase will be reported in due course (tentative composition is ~ 122). Upon further heating above 765 K *HT*-$Na_{1-x}Zn_{4-y}Sb_3$ phase reappears (also evident from DSC data, Figure S4) as a strong endothermic peak at 770 K), according to the following equation: $NaZn_4Sb_3$ + ZnSb + new → *HT*-$Na_{1-x}Zn_{4-y}Sb_3$. At around 850 K, the decomposition of *HT*-$Na_{1-x}Zn_{4-y}Sb_3$ starts according to DSC data but the melting temperature of 885 K was not achieved in the HT-PXRD data. Upon cooling, *HT*-$Na_{1-x}Zn_{4-y}Sb_3$ recovers, and with further cooling to room temperatures transforms to $NaZn_4Sb_3$, binary ZnSb, and a new phase; this transformation occurs within broad range of 760–665 K. At the end of the cooling cycle, binary ZnSb is the main product (Figure 5), which indicates that considerable Na/Zn elimination during heating at high temperatures took place, leading to the shift in composition, as schematically represented in Figure 8. DSC data of samples run in silica and alumina are in accordance with *in-situ* HT-PXRD data. More substantial shift in composition caused by more pronounced Na/Zn elimination in silica may lead to formation of intermediate side products, leading to the additional DSC-peaks on cooling. It should be noted that relative intensities of the peaks of the *HT*-$Na_{1-x}Zn_{4-y}Sb_3$ phase (apparently visible at $2\theta \sim 1.4°$ in Figure 5) vary at different temperatures, although PXRD of the quenched samples are always same. This could be due to the certain variation in composition or disorder occurring at the different temperatures, while the quenched *HT*-$Na_{1-x}Zn_{4-y}Sb_3$ always retains its stable configuration.

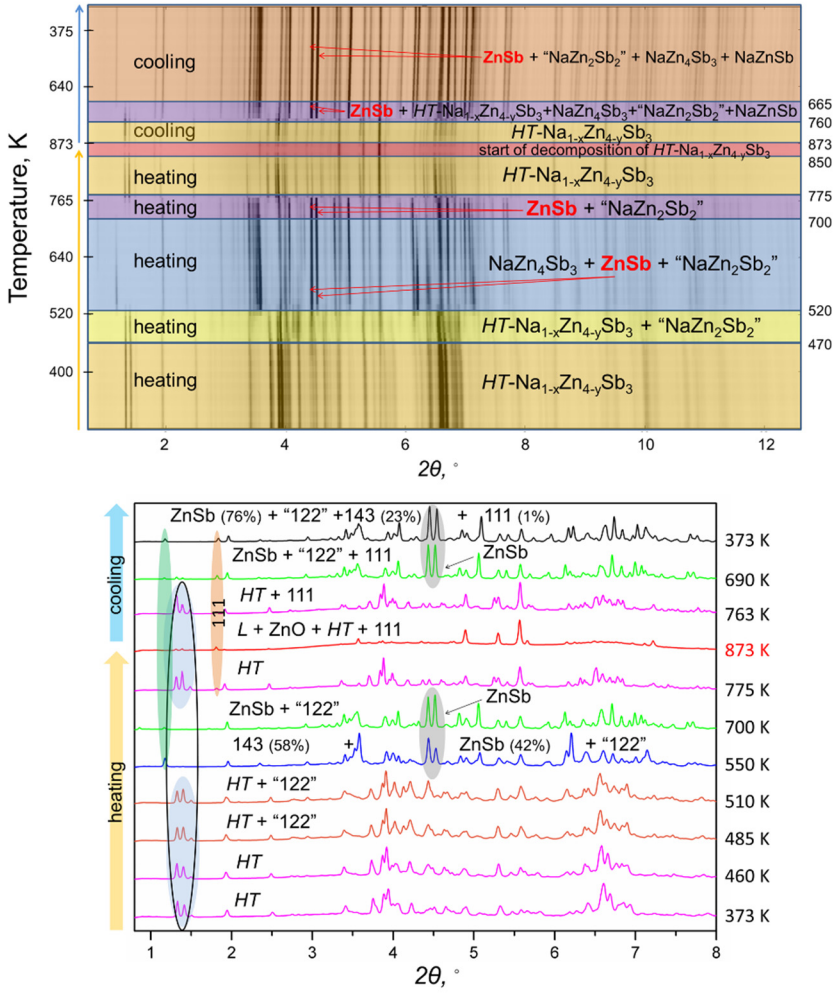

Figure 5. (Top) High-temperature *in-situ* X-ray diffraction patterns, showing the transformation of powdered sample of *HT*-$Na_{1-x}Zn_{4-y}Sb_3$ sealed into evacuated silica capillary. The "waterfall" plot shows the evolution of powder XRD patterns with the change in temperature from room temperature to 873 K followed by subsequent cooling to room temperature. The temperature regions with distinct phase contributions are highlighted in blue/yellow/purple/red/orange; (bottom) Selected high temperature powder X-ray diffraction patterns showing the products of decomposition/transformation of the *HT*-$Na_{1-x}Zn_{4-y}Sb_3$ at different temperatures. Selected groups of peaks as "fingerprints" of the ternary and binary phases are highlighted: green (143) – $NaZn_4Sb_3$; blue (*HT*) – *HT*-$Na_{1-x}Zn_{4-y}Sb_3$; orange (111) – NaZnSb; grey – ZnSb; 122 – "$NaZn_2Sb_2$".

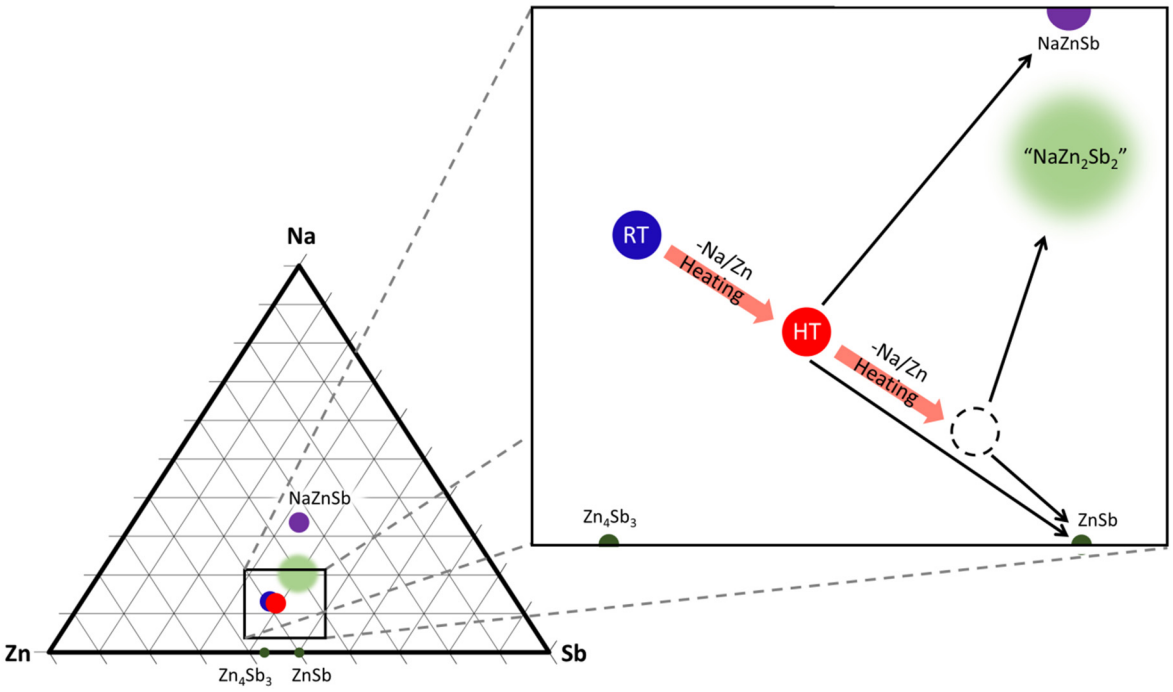

Figure 6. Schematic of the compositional ternary phase diagram for Na–Zn–Sb. Compositional shift along the line of transformation from $NaZn_4Sb_3$ (blue circle) and *HT*-$Na_{1-x}Zn_{4-y}Sb_3$ (red circle) during heating in silica capillary. The 1:4:3 composition of $NaZn_4Sb_3$ is being shifted during heating due to Na/Zn elimination, therefore the *HT*-$Na_{1-x}Zn_{4-y}Sb_3$ phase with Na/Zn depleted composition can be stabilized. The initial composition of the sample of *HT*-$Na_{1-x}Zn_4Sb_3$ phase prepared by quenching during its heating is shifted even greatly, and then unknown phase referred as "$NaZn_2Sb_2$" shows up on the phase equilibria.

Figure 6 represents schematically a compositional shift from $NaZn_4Sb_3$ to the *HT*-$Na_{1-x}Zn_{4-y}Sb_3$ and finally to the "new phase" as a result of a continuous Na/Zn elimination during heating. Upon heating, $NaZn_4Sb_3$ transforms to *HT*-$Na_{1-x}Zn_{4-y}Sb_3$, and with further heating, i.e. further Na/Zn elimination, NaZnSb appears on phase equilibria. The composition of *HT*-$Na_{1-x}Zn_{4-y}Sb_3$ phase is already Na/Zn depleted compared to that of $NaZn_4Sb_3$, therefore upon heating of *HT*-$Na_{1-x}Zn_{4-y}Sb_3$, composition further shifts allowing for the crystallization of a "$NaZn_2Sb_2$" phase together with considerable amount of binary ZnSb, indicating considerable deviation from initial 1:4:3 composition.

Elemental analysis of $NaZn_4Sb_3$ and HT-$Na_{1-x}Zn_{4-y}Sb_3$. Scanning electron microscopy (SEM) images using back-scattered electrons (BSE) and secondary electrons (SE) modes were collected for the polished pellets sintered by SPS for both $NaZn_4Sb_3$ and the *HT*-phase (Figure 7). Compositions were determined by energy-dispersive X-ray (EDX) analysis using 8–11 different areas for each sample. The elemental

distribution appears to be homogeneous, and the average compositions were found to be Na:Zn:Sb = 1.83(9):3.66(8):3.00(9) for $NaZn_4Sb_3$ and Na:Zn:Sb = 1.50(9):3.5(1):3.00(9) for *HT*-$Na_{1-x}Zn_{4-y}Sb_3$ phase, respectively. Na/Zn is overestimated because of the overlap between Na–K_α and Zn–L_α lines, leading to the difficulties in deconvoluting Na and Zn characteristic lines in the EDX spectrum. Similar inconsistency was seen for the stoichiometric NaZnSb, with Na:Zn:Sb ratio as determined by EDX 1.3:1:1 [20]. More importantly, the compositions determined by EDX analysis indicates the lower Zn and Na content in the case of *HT*-$Na_{1-x}Zn_{4-y}Sb_3$ phase as compared to $NaZn_4Sb_3$, which is consistent with the structure of *HT*-$Na_{1-x}Zn_{4-y}Sb_3$ determined from SC XRD data as well as Na/Zn depleted composition required for its synthesis.

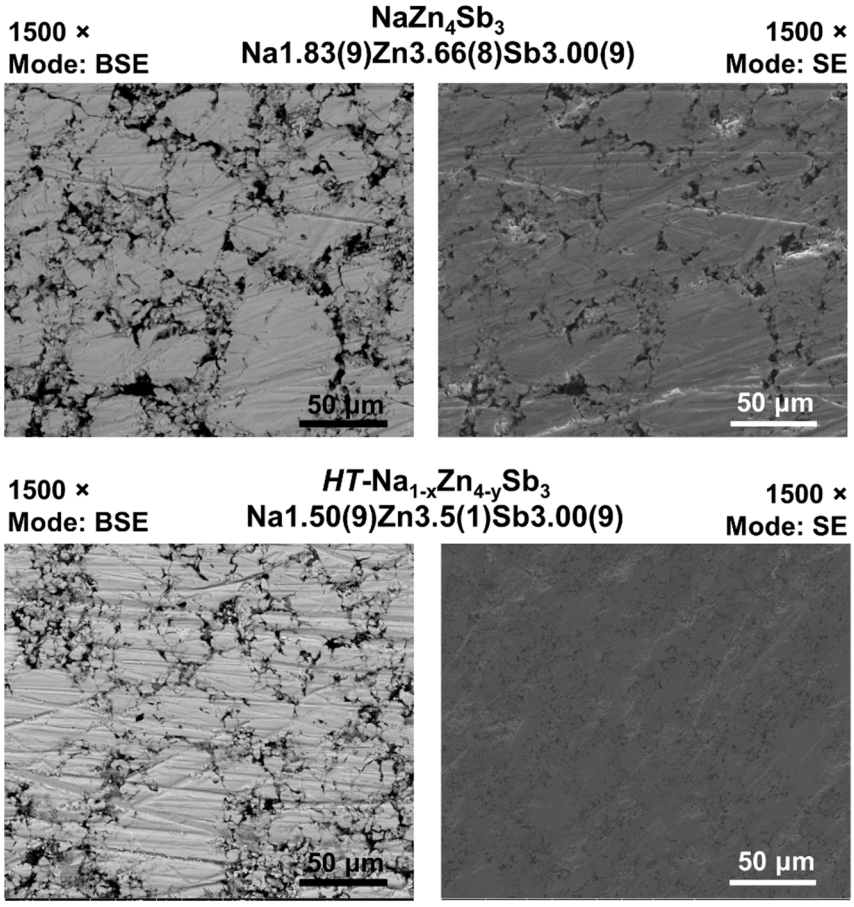

Figure 7. Scanning electron microcopy (SEM) images obtained in back-scattered electrons (BSE, left) and secondary electrons (SE, right) modes for the samples of $NaZn_4Sb_3$ (top) and *HT*-$Na_{1-x}Zn_{4-y}Sb_3$ (bottom) prepared via hydride route and further densified by SPS. The compositions of $NaZn_4Sb_3$ and *HT*-$Na_{1-x}Zn_{4-y}Sb_3$ phases determined by EDXS and averaged for the 8–11 different areas of each sample.

Low-temperature transport properties of $NaZn_4Sb_3$ and HT-$Na_{1-x}Zn_{4-y}Sb_3$. The temperature dependence of thermoelectric properties (Figure 8) in the 10–300 K temperature range has been measured for the SPS sintered pellets of $NaZn_4Sb_3$ (compactness of 85%; 7 wt. % of ZnSb impurity) and *HT*-$Na_{1-x}Zn_{4-}$

$_y$Sb$_3$ (compactness 81%). Electrical resistivities for both compounds are slightly temperature dependent but exhibit different types of behavior with increasing temperature. The electrical resistivity of the $NaZn_4Sb_3$ decreases from 2400 mΩ·cm to 1200 mΩ·cm with increasing temperature, indicative of heavily doped semiconductor. On the other hand, the electrical resistivity of *HT*-$Na_{1-x}Zn_{4-y}Sb_3$ phase is overall ~2 orders of magnitude lower than its $NaZn_4Sb_3$ counterpart and increases from 33 mΩ·cm to 36 mΩ·cm with increasing temperature, dependence similar to that of a metal.

Both materials have positive Seebeck coefficients which steadily increase with temperature up to 40 and 50 $\mu V \cdot K^{-1}$ at 300 K for *HT*-$Na_{1-x}Zn_{4-y}Sb_3$ and $NaZn_4Sb_3$ phases, respectively. This is consistent with *p*-type and holes as charge carries. Lower overall Seebeck coefficient for *HT*-$Na_{1-x}Zn_{4-y}Sb_3$ and lower electrical resistivity with the metal-like temperature dependence agree with its more metallic character, compared to $NaZn_4Sb_3$. Furthermore, the Na/Zn deficiency in *HT*-$Na_{1-x}Zn_{4-y}Sb_3$ would be responsible for more metallic nature of *HT*-$Na_{1-x}Zn_{4-y}Sb_3$ as compared to formally charge-balanced $Na^{+}(Zn^{+2})_4(Sb^{-3})_3$. Two orders of magnitude difference in resistivity for $NaZn_4Sb_3$ and *HT*-$Na_{1-x}Zn_{4-y}Sb_3$ and a subtle difference in Seebeck coefficients suggests that the variation in band structure plays a significant role in determining electronic transport of these structurally different and compositionally similar compounds.

The total thermal conductivity κ_{total} has contributions from charge carriers, κ_e (electronic thermal conductivity), and a lattice, κ_L (the lattice thermal conductivity): $\kappa_{total} = \kappa_e + \kappa_L = LT/\rho + \kappa_L$, where L is the Lorenz number and ρ is resistivity. For the metals and degenerate semiconductors with high carrier concentrations, Lorenz number approaches the Sommerfeld limit, $L = 2.45\times10^{-8}\ W\cdot\Omega\cdot K^{-2}$ (free electron model). The L estimated using experimental Seebeck coefficients [67] yields similar values of L within the $2.15 - 2.48\times10^{-8}\ W\cdot\Omega\cdot K^{-2}$ range for *HT*-$Na_{1-x}Zn_{4-y}Sb_3$ and $NaZn_4Sb_3$ phases in 300–10 K temperature range. Thus, the conservative value of $L = 2.45\times10^{-8}\ W\cdot\Omega\cdot K^{-2}$ was used. The estimated contribution of electronic thermal conductivity into total thermal conductivity is less 0.1% and less the 2.5% of for $NaZn_4Sb_3$ and *HT*-$Na_{1-x}Zn_{4-y}Sb_3$ phases, respectively. The thermal conductivity of both phases increases with temperature from 0.2 $W\cdot m^{-1}\cdot K^{-1}$ to 0.9 $W\cdot m^{-1}\cdot K^{-1}$ at 300 K. Both $NaZn_4Sb_3$ (N_{cell} = 16 atoms; V_{cell} = 394.2 Å^3) and structurally more complex *HT*-$Na_{1-x}Zn_{4-y}Sb_3$ (N_{cell} = 192 atoms; V_{cell} = 5986.1 Å^3) have low thermal conductivity. The layered structure of $NaZn_4Sb_3$ may favor a high density of stacking faults similar to the $SrZnSb_2$, where the boundary scattering was found to reduce thermal conductivity by approximately 30% at room temperature as compared to structurally related $SrZn_2Sb_2$ [31-32]. Additionally, the low thermal conductivity could partially be attributed to the lower pellet densities of measured samples (81% and 85%). Moreover, both compounds are lacking the peak in thermal conductivity at lower temperatures. Such a peak is typical for temperature dependence of thermal conductivity of crystalline insulating/semiconducting solids [68-69].

Such "glass-like" temperature dependence of thermal conductivity, typical for amorphous materials, suggests that the disordered complex crystal structure as in *HT*-$Na_{1-x}Zn_{4-y}Sb_3$, and "rattling" of Na atoms in the interlayer space in the crystal structure of $NaZn_4Sb_3$ (Na atom has large ADPs, Table 2) can be responsible for the phonon scattering at low temperatures.

The thermoelectric figure-of-merit *zT* at room temperature amounts to 7.3×10^{-5} for $NaZn_4Sb_3$ and to 1.4×10^{-3} for *HT*-$Na_{1-x}Zn_{4-y}Sb_3$. the low *zT* for both compounds can be attributed to low Seebeck coefficient and high electrical resistivity, especially in the case of formally charge balanced $NaZn_4Sb_3$. Aliovalent substitutions in $NaZn_4Sb_3$ compound (for instance Na for Ca) may lead for increase of carrier concentration and decrease of its high resistivity.

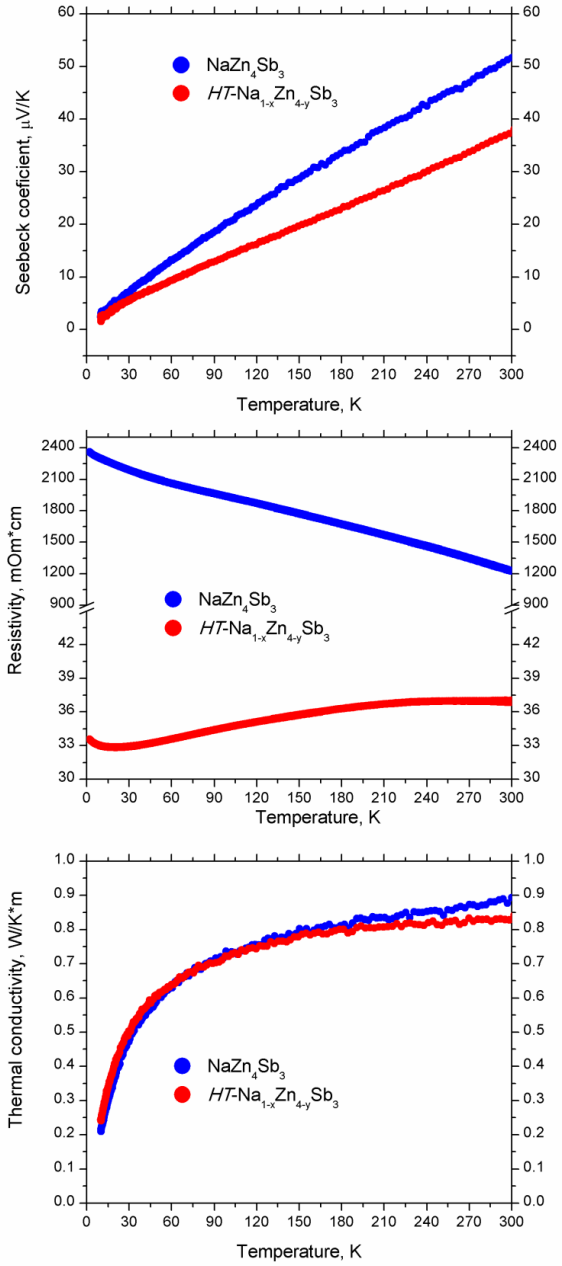

Figure 8. Temperature dependence of transport properties for $NaZn_4Sb_3$ (blue) and *HT*-$Na_{1-x}Zn_{4-y}Sb_3$ (red): (top) electrical resistivity; (middle) Seebeck coefficient, (bottom) thermal conductivity (the estimated electronic thermal conductivity contribution is negligible less than 0.1% for $NaZn_4Sb_3$ phase and less than 2.5% for *HT*-$Na_{1-x}Zn_{4-y}Sb_3$ phase).

Conclusions.

In-situ synchrotron powder diffraction analysis provided a "panoramic view" on the ternary phases in the Na–Zn–Sb system. Two compositionally similar, but structurally different phases $NaZn_4Sb_3$ and *HT*-$Na_{1-x}Zn_{4-y}Sb_3$ were detected on phase equilibria below and above 736 K, respectively. The *HT*-phase can be prepared by quenching samples from high temperatures only if Na- and Zn-depleted composition is used for synthesis. Moreover, *in-situ* powder X-ray diffraction experiments show an additional ternary phase, stabilized due to considerable Na/Zn elimination under vacuum at elevated temperatures. The structure and properties of this phase will be reported in due course. Transport properties of $NaZn_4Sb_3$ and *HT*-$Na_{1-x}Zn_{4-y}Sb_3$ phases show low thermal conductivities at room temperature of 0.9 $W \cdot m^{-1} \cdot K^{-1}$. Both polymorphs exhibit moderate positive Seebeck coefficients of 40-50 $\mu V \cdot K^{-1}$ at 300 K, indicative of *p*-type conduction. The observed resistivities differs by two orders of magnitude, possibly indicating complex transport behaviors. The presented here synthetic hydride approach coupled with *in-situ* high-temperature powder X-ray diffraction allows for the fast compositional and temperature screening of the phase space, leading to the discovery of the phases, stable in a narrow compositional and temperature range.

Associated content.

Supporting Information. Additional Tables with interatomic distances, Rietveld refinement plots and Tables with parameters of XRD data collection and refinement can be found in the Supporting Information. This material is available free of charge via the Internet at http://pubs.acs.org.

Funding Sources

The financial support for J.V.Z. startup funds from Iowa State University is gratefully acknowledged. The work at Ames Laboratory was supported by the U.S. Department of Energy (DOE), Office of Science, Basic Energy Sciences, Materials Science and Engineering Division, under Contract No. DE-AC02-07CH11358, including a grant of computer time at the National Energy Research Scientific Computing Center (NERSC) in Berkeley, CA. Use of the Advanced Photon Source at Argonne National Laboratory was supported by the U. S. Department of Energy, Office of Science, Office of Basic Energy Sciences, under Contract No. DE-AC02-06CH11357.

Notes

Authors declare no competing financial interest.

Author information.

Corresponding Author

* yzaikina@iastate.edu

Notes: The authors declare no competing financial interest.

Acknowledgements. We thank Dr. Arkady Ellern (Department of Chemistry, Iowa State University) for the help with SC XRD data collection, Dr. Kirill Kovnir (Department of Chemistry, Iowa State University and US-DOE Ames Laboratory) for the access to DSC-TG and PPMS, Warren Straszheim (Materials Analysis Research Laboratory, Iowa State University) for the help with SEM/EDXS measurement. Dr. Wenqian Xu and Dr. Andrey Yakovenko at 17-BM beamline, APS ANL, for help with high-temperature synchroton powder XRD data collection.

References

[1] Gautier, R.; Zhang, X.; Hu, L.; Yu, L.; Lin, Y.; Sunde, T. O. L.; Chon, D.; Poeppelmeier, K. R.; Zunger, A. Prediction and accelerated laboratory discovery of previously unknown 18-electron ABX compounds. *Nature Chem*. **2015**, *7*, 308–316.

[2] Curtarolo, S.; Hart, G. L. W.; Nardelli, M. B.; Mingo, N.; Sanvito, S.; Levy, O. The high-throughput highway to computational materials design. *Nat. Mater.* **2013**, *12*, 191–201.

[3] Haynes, A. S.; Stoumpos, C. C.; Chen, H.; Chica, D.; Kanatzidis, M. G. Panoramic Synthesis as an Effective Materials Discovery Tool: The System Cs/Sn/P/Se as a Test Case. *J. Am. Chem. Soc.* **2017**, *139*, 10814–10821.

[4] Jansen, M. Conceptual Inorganic Materials Discovery – A Road Map. *Adv. Mater*. **2015**, *27*, 3229–3242.

[5] Alberi, K. *et. al*. The 2019 materials by design roadmap. *J. Phys. D: Appl. Phys.* **2019**, *52*, 013001.

[6] Oliynyk, A. O.; Antono, E.; Sparks, T. D.; Ghadbeigi, L.; Gaultois, M. W.; Meredig, B.; Mar, A. High-Throughput Machine-Learning-Driven Synthesis of Full-Heusler Compounds. *Chem. Mater*. **2016**, *28*, 7324–7331.

[7] Gvozdetskyi, V.; Bhaskar, G.; Batuk, M.; Zhao, X.**;** Wang, R.; Carnahan, S.L.; Hanrahan, M.P.; Ribeiro, R.A.; Canfield, P.C.; Rossini, A.J.; Wang, C.-Z.; Ho, K.-M.; Hadermann, J.; Zaikina, J.V. Computationally-

driven discovery of a family of layered LiNiB polymorphs. *Angew. Chem. Int. Ed.* **2019**, DOI: 10.1002/anie.201907499 and 10.1002/ange.201907499

[8] Shoemaker, D. P.; Hu, Y. J.; Chung, D. Y.; Halder, G. J.; Chupas, P. J.; Soderholm, L.; Mitchell, J. F.; Kanatzidis, M. G. In situ studies of a platform for metastable inorganic crystal growth and materials discovery. *PNAS.* **2014**, *111*, 10922–10927.

[9] Kanatzidis, M. G. Discovery-Synthesis, Design, and Prediction of Chalcogenide Phases. *Inorg. Chem.* **2017**, *56*, 3158–3173.

[10] Cheong, S.; Watt, J.; Ingham, B.; Toney, M. F.; Tilley, R. D. In situ and ex situ studies of platinum nanocrystals: growth and evolution in solution. *J. Am. Chem. Soc.* **2009**, *131*, 14590–14595.

[11] Bai, J.; Hong J.; Chen, H.; Graetz, J.; Wang, F. Solvothermal synthesis of $LiMn_{1-x}Fe_xPO_4$ cathode materials: a study of reaction mechanisms by time-resolved in situ synchrotron X-ray diffraction. *J. Phys. Chem. C* **2015**, *119*, 2266–2276.

[12] Jensen, K. M. O.; Tyrsted, C.; Bremholm, M.; Iversen B. B. In situ studies of solvothermal synthesis of energy materials *Chem. Sus. Chem*. **2014**, 7, 1594–1611.

[13] Woo, K. E.; Wang, J.; Wu, K.; Lee, K.; Dolyniuk, J.-A.; Pan, S.; Kovnir. K. Mg-Si-As: An Unexplored System with Promising Nonlinear Optical Properties. *Adv. Funct. Mater*. **2018**, *28*, 1801589.

[14] Owens-Baird, B.**;** Lee, S.; Kovnir K. Two-dimensional metal $NaCu_{6.3}Sb_3$ and solid-state transformations of sodium copper antimonides. *Dalton Trans*., **2017**, 46, 12438.

[15] Hudak, B. M.; Depner, S. W.; Waetzig, G. R.; Talapatra, A.; Arroyave, R.; Banerjee, S.; Guiton, B. S. Real-time atomistic observation of structural phase transformations in individual hafnia nanorods. *Nature Comm*. **2017**, *8*, 15316.

[16] Ma, T.; Wang, S.; Chen, M.; Maligal-Ganesh, R. V.; Wang, L.-L.; Johnson, D. D.; Kramer, Matthew J.; Huang, W.; Zhou, L. Toward Phase and Catalysis Control: Tracking the Formation of Intermetallic Nanoparticles at Atomic Scale. *Chem.* **2019**, *5*, 1235–1247.

[17] Vasquez, G.; Huq, A.; Latturner, S. E. In Situ Neutron Diffraction Studies of the Metal Flux Growth of Ba/Yb/Mg/Si Intermetallics. *Inorg. Chem.* **2019**, 58, 8111–8119.

[18] Schmidt, J.; Schnelle, W.; Grin, Y.; Kniep, R. Pulse plasma synthesis and chemical bonding in magnesium diboride. *Solid State Sci.* **2003**, *5*, 535–539.

[19] Gvozdetskyi, V.; Hanrahan, M. P.; Ribeiro, R. A.; Kim, T.; Zhou, L.; Rossini, A. J.; Canfield, P. C.; Zaikina, J. V. Hydride route to alkali metal borides: a case study of lithium nickel borides. *Chem. Eur. J.* **2019**, *25*, 4123–4135.

[20] Cox, T.; Gvozdetskyi, V.; Owens-Baird, B.; Zaikina, J. V. Rapid phase screening via hydride route: a discovery of $K_{8-x}Zn_{18+3x}Sb_{16}$. *Chem. Mater.* **2018**, *30*, 8707–8715.

[21] Gvozdetskyi, V.; Owens-Baird, B.; Hong, S.; Zaikina, J. V. Thermal stability and thermoelectric properties of NaZnSb. *Materials.* **2019**, *12*, 48–62.

[22] Zaikina, J. V.; Batuk, M.; Abakumov, A. M.; Navrotsky, A.; Kauzlarich, S. M. Facile Synthesis of $Ba_{1-x}K_xFe_2As_2$ Superconductors via Hydride Route. *J. Am. Chem. Soc.* **2014**, *136*, 16932–16939.

[23] Zaikina, J. V.; Kwong, M. Y.; Baccam, B.; Kauzlarich, S. M. Superconductor-in-an-hour: Spark Plasma synthesis of Co and Ni-doped $BaFe_2As_2$. *Chem. Mater*. **2018**, *30*, 8883–8890.

[24] Ma, X.; Xu, F.; Atkins, T. M.; Goforth, A. M.; Neiner, D.; Navrotsky, A.; Kauzlarich, S. M. A versatile low temperature synthetic route to Zintl phase precursors: Na_4Si_4, Na_4Ge_4 and K_4Ge_4 as examples. *Dalton Trans*. **2009**, *0*, 10250–10255.

[25] Yi, T.; Chen, S.; Li, S.; Yang, H.; Bux, S.; Bian, Z.; Katcho, N. A.; Shakouri, A.; Mingo, N.; Fleurial, J. P.; Browning, N. D.; Kauzlarich, S. M. Synthesis and characterization of Mg_2Si/Si nanocomposites prepared from MgH_2 and silicon, and their thermoelectric properties. *J. Mater. Chem.* **2012**, *22*, 24805–24813.

[26] Janka, O.; Zaikina, J. V.; Bux, S. K.; Tabatbaifar, H.; Yang, H.; Browing, N. D.; Kauzlarich, S. M. Microstructure investigations of Yb- and Bi-doped Mg_2Si prepared from metal hydrides for thermoelectric applications *J. Solid State Chem*. **2017**, *245*, 152–159.

[27] Sui, F.; Kauzlarich, S. M. Tuning Thermoelectric Properties of Type I Clathrate $K_{8-x}Ba_xAl_{8+x}Si_{38-x}$ through Barium Substitution. *Chem. Mater.* **2016,** *28*, 3099–3107.

[28] Perez, C. J.; Bates, V. J.; Kauzlarich, S. M. Hydride Synthesis and Thermoelectric Properties of Type-I Clathrate $K_8E_8Ge_{38}$ (*E* = Al, Ga, In). *Inorg. Chem.* **2019**, *58*, 1442–1450.

[29] Kauzlarich, S.M. Chemistry, structure, and bonding of Zintl phases and ions. VCH Publishers Inc., New York, USA **1996.**

[30] Fässler, T. F. Zintl phases: principles and recent developments. Book Series: Structure and Bonding Springer-Verlag Berlin: Heidelberg, Germany **2011,** 139.

[31] Kauzlarich, S. M.; Zevalkink, A.; Toberer, E.; Snyder, G.J. Zintl phases: recent developments in thermoelectrics and future outlook. In *Thermoelectric materials and devices*. Nandhakumar, I.; White, M. M.; Beeby, S., Eds.; Book Series: RSC Energy and Environment Series. The Royal Society of Chemistry: London, United Kingdom **2017**, 17, 1–26.

[32] Kazem, N.; Kauzlarich, M. Thermoelectric properties of Zintl antimonides. In *Handbook on the physics and chemistry of rare earth.* Bünzli, J.-C. G.; Pecharsky, V. K. North Holland: Amsterdam, Netherlands **2016**, 50, 177–208.

[33] Toberer, E. S.; May, A. F.; Snyder, G. J. Zintl chemistry for designing high efficiency thermoelectric materials. *Chem. Mater.* **2010**, *22*, 624–634.

[34] Gascoin, F.; Ottensmann, S.; Stark, D.; Haile, S. M.; Snyder, G. J. Zintl phases as thermoelectric materials: Tuned transport properties of the compounds $Ca_xYb_{1-x}Zn_2Sb_2$. *Adv. Funct. Mater.* **2005**, *15*, 1860–1864.

[35] Toberer, E. S.; May, A. F.; Melot, B. C.; Flage-Larsend, E.; Snyder, G. J. Electronic structure and transport in thermoelectric compounds $A Zn_2Sb_2$ (*A* = Sr, Ca, Yb, Eu). *Dalton Trans.* **2010**, *39*, 1046–1054.

[36] Brown, S. R.; Kauzlarich, S. M.; Gascoin, F.; Snyder, G. J. $Yb_{14}MnSb_{11}$: New high efficiency thermoelectric material for power generation. *Chem. Mater*. **2006**, *18*, 1873–1877.

[37] Hu, Y.; Cerretti, G.; Kunz Will, E. L.; Bux, S. K.; Kauzlarich, S. M. The remarkable crystal chemistry of the $Ca_{14}AlSb_{11}$ structure type, magnetic and thermoelectric properties. *J. Solid State Chem.* **2019**, 271, 88–102.

[38] PDXL: Integrated X-ray powder diffraction software, Version 2.8.1.1. Rigaku, **2018**.

[39] Apex3, Version 2017.3, Bruker, USA.

[40] Sheldrick, G. M. A short history of SHELX. *Acta Cryst*. **2008**, *A64*, 112–122.

[41] Spek, A. L. Structure validation in chemical crystallography. *Acta Cryst.* **2009**, *D65*, 148–155.

[42] Boyle, P. D. *COSET*: a program for deriving and testing merohedral and pseudo-merohedral twin laws. *J. Appl. Cryst*. **2014**, *47*, 467–470.

[43] Chupas, P. J.; Chapman, K. W.; Kurtz, C.; Hanson, J. C.; Lee, P. L.; Grey, C. P. A versatile sample-environment cell for non-ambient X-ray scattering experiments. *J. Appl. Cryst*. **2008**, *41*, 822–824.

[44] Toby, B. H.; Von Dreele, R. B. GSAS-II: the genesis of a modern open-source all purpose crystallography software package. *J. Appl. Cryst*. **2013**, *46*, 544–549.

[45] Kresse, G.; Furthmuller, J. Efficiency of ab-initio total energy calculations for metals and semiconductors using a plane-wave basis set. *Comp. Mater. Sci*. **1996**, *6*, 15–50.

[46] Kresse, G.; Furthmuller, J. Efficient iterative schemes for ab initio total-energy calculations using a plane-wave basis set. *Phys. Rev. B* **1996**, *54*, 11169–11186.

[47] Kresse, G.; Joubert, D. From ultrasoft pseudopotentials to the projector augmented-wave method. *Phys. Rev. B* **1999**, *59*, 1758–1775.

[48] Bloechl, P. E. Projector augmented-wave method. *Phys. Rev. B* **1994**, *50*, 17953–17979.

[49] Perdew, J. P.; Burke, K.; Ernzerhof, M. Generalized Gradient Approximation Made Simple. *Phys. Rev. Lett.* **1996**, *77*, 3865–3868.

[50] Kahlert, H.; Schuster, H. U.; Ternary phases of sodium or potassium with elements of 2B-group and 5B-group. *Z. Naturforsch. B* **1976**, 31, 1538–1539.

[51] Savelsberg, G.; Schaefer, H. On Ternary Pnictides and Chalkogenides of Alkaline Metals and IB-resp. II B-Elements (*in German*) *Z. Naturforsch. B* **1978**, *33*, 370–373.

[52] Snyder, G. J.; Christensen, M.; Nishibori, E.; Caillat, T.; Iversen, B. B. Disordered zinc in Zn_4Sb_3 with phonon-glass and electron-crystal thermoelectric properties. *Nature Mater.* **2004**, *3*, 458–463.

[53] Nylén, J.; Andersson, M.; Lidin, S.; Häussermann, U. The Structure of α-Zn_4Sb_3: Ordering of the Phonon-Glass Thermoelectric Material β-Zn_4Sb_3. *J. Am. Chem. Soc.* **2004**, *126, 50*, 16306–16307.

[54] Mozharivskyj Y.; Janssen, Y.; Harringa, J. L.; Kracher, A.; Tsokol, A. O.; Miller, G. J. $Zn_{13}Sb_{10}$: A Structural and Landau Theoretical Analysis of Its Phase Transitions. *Chem. Mater*. **2006**, *183*, 822–831.

[55] Nylén, J.; Lidin, S.; Andersson, M.; Iversen, B. B.; Newman, N.; Häussermann, U. Low-Temperature Structural Transitions in the Phonon-Glass Thermoelectric Material β-Zn_4Sb_3: Ordering of Zn Interstitials and Defects. *Chem. Mater.* **2007**, *194*, 834–838.

[56] Lo, C. W. T.; Svitlyk, V.; Chernyshov, D.; Mozharivskyj, Y. The updated Zn–Sb phase diagram. How to make pure $Zn_{13}Sb_{10}$ ("Zn_4Sb_3"). *Dalton Trans.* **2018**, *47*, 11512–11520.

[57] ICSD – the Inorganic Crystal Structure Database, FIZ – Karlsruhe, **2018**.

[58] Schroeder, G.; Schuster, H. U. LiZnSb, an additional ternary phase with a Wurzit-type lattice (*in German*) *Z. Naturforsch. B* **1975**, *30*, 978–979.

[59] He, H.; Stoyko, S. S.; Mar, A.; Bobev, S. Ternary $K_2Zn_5As_4$-type pnictides $Rb_2Cd_5As_4$ and $Rb_2Zn_5Sb_4$, and the solid solution $Rb_2Cd_5(As,Sb)_4$. *Acta Cryst. C* **2013**, *69*, 455–459.

[60] Carter, F. L.; Mazelsky, R. The ZnSb structure; A further enquiry. *J. Phys. and Chem. of Solids,* **1964**, *25*, 571–581

[61] Wang, J.; Kovnir, K. Elusive β-Zn_8Sb_7: A New Zinc Antimonide Thermoelectric. *J. Am. Chem. Soc.* 2015,137, 39, 12474–12477.

[62] He, H.; Tyson, C.; Bobev, S. Eight-Coordinated Arsenic in the Zintl Phases $RbCd_4As_3$ and $RbZn_4As_3$: Synthesis and Structural Characterization. *Inorg. Chem*. **2011**, *50*, 8375–8383.

[63] Cordier, G.; Ochmann, H. Crystal structure of trisodium tectodiantimonidoindate, Na_3InSb_2. *Zeitschrift für Kristallographie*. **2010**, *195*, 107–108.

[64] Cordier, G.; Ochmann, H.; Schaefer, H. $Na_2Al_2Sb_3$ und $K_2Al_2Sb_3$, zwei neue Zntlphasen mit Schichtanionen. *Revue de Chimie Minerale*. **1984**, *21*, 282–291.

[65] Eisenmann, B.; Klein, J. Na_5SnSb_3 and K_8SnSb_4, zwei neue Zintlphasen mit tetraedrischen $SnSb_4$-Baueinheiten. *Z. Naturforsch. B.* **1988**, *43*, 1156–1160.

[66] Carrillo Cabrera, W.; Caroca Canales, N.; Von Schnering, H.G. Dipotassium Sodium Diantimonidoindate, $K_2Na[InSb_2]$, a compound with the polyanion $^2_\infty[In_2Sb_2Sb_{4/2}]^{6-}$. *Z. anorg. allg. Chem*. **1993**, *619*, 1717–1720.

[67] Saparov, B.; Saito, M.; Bobev, S. Syntheses, and crystal and electronic structures of the new Zintl phases Na_2ACdSb_2 and K_2ACdSb_2(*A* = Ca, Sr, Ba, Eu, Yb): Structural relationship with Yb_2CdSb_2 and the solid solutions $Sr_{2-x}A_xCdSb_2$, $Ba_{2-x}A_xCdSb_2$ and $Eu_{2-x}Yb_xCdSb_2$. *J. Solid State Chem*. **2011**, *184*, 432–440.
[68] Kim, H. S.; Gibbs, Z. M.; Tang, Y.; Wang, H.; Snyder, G.J. Characterization of Lorenz number with Seebeck coefficient measurement. *APL Mater.* **2015**, *3*, 041506–041511.
[69] Stefanoski, S.; Beekman, M.; Nolas, G.S. Inorganic Clathrates for Thermoelectric Applications. In: Nolas G. (eds) The Physics and Chemistry of Inorganic Clathrates. Springer Series in Materials Science, vol 199, Ch. 6, 169–191, Springer, Dordrecht, **2014.**
[70] Cohn, J. L.; Nolas, G. S.; Fessatidis, V.; Metcalf, T. H.; Slack, G. A. Glasslike Heat Conduction in High-Mobility Crystalline Semiconductors. *Phys. Rev. Lett.* **1999**, *82*, 779–782.

TOC image

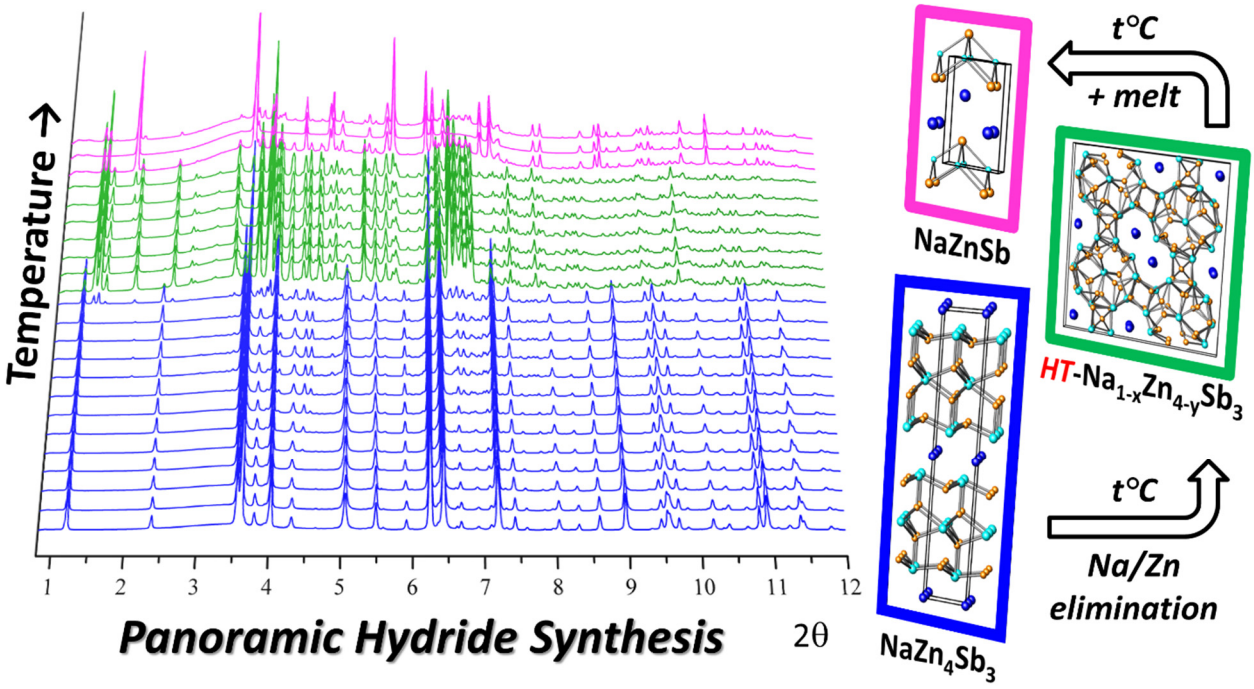
Temperature →
1
2
3
4
5
6
7
8
9
10
11
12
Panoramic Hydride Synthesis
2θ
t°C
+ melt
NaZnSb
HT-Na1-xZn4-ySb3
t°C
Na/Zn
elimination
NaZn4Sb3